Elastic properties and mechanical stability of chiral and filled viral capsids

Mathias Buenemann and Peter Lenz
Fachbereich Physik, Philipps-Universität Marburg, D-35032 Marburg, Germany
(Received 28 July 2008; revised manuscript received 19 September 2008; published 25 November 2008)

The elasticity and mechanical stability of empty and filled viral capsids under external force loading are studied in a combined analytical and numerical approach. We analyze the influence of capsid structure and chirality on the mechanical properties. We find that generally skew shells have lower stretching energy. For large Föppl–von Kármán numbers γ ($\gamma \approx 10^5$), skew structures are stiffer in their elastic response than nonchiral ones. The discrete structure of the capsules not only leads to buckling for large γ but also influences the breakage behavior of capsules below the buckling threshold: the rupture force shows a $\gamma^{1/4}$ scaling rather than a $\gamma^{1/2}$ scaling as expected from our analytical results for continuous shells. Filled viral capsids are exposed to internal anisotropic pressure distributions arising from regularly packaged DNA coils. We analyze their influence on the elastic properties and rupture behavior and we discuss possible experimental consequences. Finally, we numerically investigate specific sets of parameters corresponding to specific phages such as $\phi 29$ and cowpea chlorotic mottle virus (CCMV). From the experimentally measured spring constants we make predictions about specific material parameters (such as bending rigidity and Young's modulus) for both empty and filled capsids.

DOI: 10.1103/PhysRevE.78.051924 PACS number(s): 87.10.Pq, 87.80.Fe, 87.16.ad

I. INTRODUCTION

With modern experimental methods it has become possible to probe the elastic and mechanical properties of living matter on the single cell and molecular level. Important examples include (i) the stiffness of polymerized actin networks [1,2], (ii) active mechnical response of cells [3], (iii) protein unfolding in single-molecule experiments [4], and (iv) the robustness of viral capsids measured by scanning force microscopy (SFM) experiments [5,6].

The latter studies are motivated by the astonishing elastic properties of phages which allow them to withstand the high internal pressures exerted by their densely packed DNA. This pressure is necessary to inject the DNA into the prokaryotic host cell [7].

In typical SFM studies the phage capsids are indented on the nanometer scale with a tip which is mounted to a flexible cantilever [5,6]. The tip radius is typically less than 20 nm [5]. For small forces one generally observes a reversible *elastic* behavior. The measured data are force-distance curves which are characterized by a distribution of spring constants. Larger forces may cause the shell to weaken irreversibly in a small region. This softening is commonly attributed to the failure of individual capsomer-capsomer bonds and local disintegration of the shell. Rupture experiments carried out on phage $\phi 29$ show that these capsids resist external point forces up to ~ 1 nN.

These experimental methods have successively been refined and have analyzed the effect of capsid maturation on shell stiffness [8], and the influence of DNA packing [9,10]. In the most recent experiments it has even been possible to probe specific loci on the shell surface [10].

Crick and Watson [11] argued that, because of their small genome size, viruses can encode just a small number of different capsid proteins, so called capsomers. Due to the small variety in constituents the shell must be arranged in a very regular fashion. Indeed, in spherical viruses the capsomers are located on the vertex positions of an equilateral triangulation of a sphere [12]. While a planar triangulated sheet consists exclusively of vertices with six neighbors ("hexamers"), the spherical topology of viral shells introduces local defects in the triangulation. Upon closing the triangulated sheet to a spherical shape one must, due to Euler's theorem, insert at least twelve capsomers with five neighbors ("pentamers"). These pentamers lie on the vertex positions of a perfect icosahedron and the capsids of spherical viruses have icosahedral symmetry [13,14].

More precisely, the centers of the capsomers are the vertices of an icosadeltahedron, which can be characterized by the Caspar-Klug numbers h and k [12]. These numbers have a direct geometrical interpretation: to get from one pentamer to its nearest neighboring pentamer, one must follow a straight chain of h capsomers, then make a 60° turn and proceed along another straight chain of k capsomers. We refer to capsids with $h,k \neq 0$ as *skew* capsids. Moreover, skew capsids with $h \neq k$ are *chiral*. The number of capsomers needed to build a (h,k) capsid is $10T+2$, where $T=h^2+hk+k^2$ is the so-called triangulation number [12]. A given triangulation number might have several realizations (h,k); see Table I. In particular, for $T=49,147,169$ both skew and non-

TABLE I. Selected triangulation numbers T with more than one (h,k) realization. It follows from the definition of T that $T=49$ is the smallest triangulation number with more than one realization.

T	(h,k)
49	(5,3); (7,0)
91	(6,5); (9,1)
133	(9,4); (11,1)
147	(7,7); (11,2)
169	(8,7); (13,0)
1183	(26,13); (29,9); (31,6)

skew structures can be realized. Examples are the *Paramecium bursaria Chlorella* virus type 1 (PBCV1) with triangulation number $T=169$ and its skew realization $(h,k)=(8,7)$ [15] and the *Chilo* iridescent virus (CIV) with $T=147$ and its $(h,k)=(7,7)$ realization [16]. The triangulation number of the giant mimivirus [17] is estimated to be around $T \approx 1179$. The closest theoretically valid triangulation number is $T=1183$, which has three possible (h,k) pairs.

Of course, not all viruses are spherical. For example, the lentivirus HIV-1 has a conical shape [18]. Some bacteriophages like $\phi 29$ [19] and $T4$ mutants [20] have a spherocylindrical shape. Recent numerical studies [21,22] suggest that such complex shapes are the result of a spontaneous curvature.

The elasticity of these viral capsids can be, as mentioned, probed in SFM experiments, which show that for small deformations the elastic response is fully reversible. As shown here in detail, this behavior can be fully explained in the framework of continuum shell mechanics. In this work we present analytical results for the linear response of thin spherical shells. The elastic behavior of such shells arises from the competition between in-plane stretching and bending. The strength of these contributions is set by the two-dimensional (2D) Young's modulus κ_e and the bending rigidity κ_b. The elasticity of a shell of radius R can then be characterized by the dimensionless Föppl–von Kármán (FvK) number $\gamma \equiv R^2 \kappa_e / \kappa_b$. Our analytical results hold for viral capsids in the limit of small γ.

At larger γ the applicability of continuum theory to viral shells is limited by the discrete structure of capsids. The disclinations must be treated as local defects of the otherwise isotropic capsid material. For flat sheets local defects can be incorporated into von Kármán's plate equations [23]. It turns out that above a threshold at $\gamma_b \simeq 154$ pentamers buckle out, giving the sheet a conical shape. The buckling transition has been shown to have strong influence on the shape [24] and elasticity [25,26] of viral capsids.

Generally speaking, the distribution of strain is changed by the presence of disclinations. For small γ the influence of in-plane deformation is small compared to bending. Therefore the altered strain distribution becomes effective only for large strains, i.e., for large deformations. For $\gamma > \gamma_b$ in-plane strain dominates the elasticity and even the small-deformation regime is strongly influenced by the presence of disclinations.

Most viruses have FvK numbers $\gamma \simeq 10^2$ and are in the order of the buckling threshold. Bacteriophages, like the widely studied $\phi 29$ or $T4$, typically have $\gamma \simeq 10^3$. Among viruses the giant mimivirus with $\gamma \simeq 10^4$ has a very large value. However, FvK numbers as high as $\gamma \simeq 10^6$ have been realized with polyelectrolyte capsules [27,28].

The analytical tools employed in this work do not cover the regime of buckled icosahedral shells. Even for small γ they are limited to small deformations. Unfortunately, it is not straightforward to extend the analytic scheme presented in Ref. [23] to curved surfaces. However, by making use of an advanced discretization scheme we can treat large γ and strong deformations numerically. Here, we present numerical results on the influence of buckling on the reversible and irreversible elastic properties of empty and filled viral capsids. In particular, the influence of the triangulation number and its different realizations on the elastic behavior of capsids is analyzed.

Phage capsids contain densely packed DNA which exerts an enormous force on the shell. Values as high as 6 MPa have been estimated for $\phi 29$ based on the measurements of the stall force of the packing machinery [29]. Experiments and analytical models on phage λ, in which the genome ejection is osmotically inhibited, also report internal pressures in the order of 5 MPa [30,31]. There is experimental [32,33] and numerical [34] evidence that inside the capsids the DNA is organized in regular coils, leading to significant effects on the energetics of DNA packing [35]. Here, we show that coiled DNA leads to an anisotropic pressure which (under high-salt conditions) strongly influences the rupture behavior.

Our theoretical predictions on the mechanical strength of capsids might be relevant for the following experimental situations: (i) Experiments usually carried out in buffer solutions with different salt concentrations. The mean DNA pressure as well as the anisotropy strongly depend on these concentrations. Our numerical results may help to separate the pressure dependence of mechanical strength from the influence of bond softening due to different buffer conditions. (ii) Osmotic shock experiments; this is a common technique to extract DNA from viral capsids. With the aid of our numerics we can determine the critical internal pressure needed to break the capsid.

In our numerical simulation we model the viral capsid as a triangulated spherical surface. We are able to construct icosadeltahedra with arbitrary triangulation (h,k) and to implement specific phage geometries. For the bending energy we use a fairly novel discretization scheme that is based on a direct geometrical interpretation of the mean curvature [36]. The advantage of this approach is its validity even for strongly deformed surfaces.

A similar discretization scheme, originally introduced for the simulation of crystalline membranes [37], has been used to study the dependence of virus shape on the FvK number [24] and the effect of DNA packing and maturation on viral shape [38]. Only recently, the elasticity of capsids has come into the focus of such numerical studies [39]. In a short communication [25] we have already applied our approach to study the elastic properties and mechanical stability of viral capsids under external force loading. Here, we give more details of this analysis, extend it to chiral capsids and present new analytical results.

This paper is organized as follows. In the next section, we present our analytical results. After introducing our numerical approach in Sec. III this method is applied to empty and filled capsids of different geometries in Sec. IV. The paper ends with a summary and outlook.

II. ANALYTICAL RESULTS

In this section we first introduce the elastic description of the viral capsid and then present analytical results for the elastic response to point deformations. In doing so, we use a continuum approach which does not take into account the topological defects of the spherical shell.

A. Continuum approach

Viral shells are built of morphological protein units ("capsomers") giving the shell a discrete structure. As pointed out by Caspar and Klug [12], these capsomers represent a regular triangulation of the sphere. The morphological units are held together by covalent bonds. Because of the geometrical constraint that the capsomers have to arrange on a closed spherical surface the bonds have nonoptimal length and angles. These deviations from the optimal planar conformation give rise to bending and stretching energy even in the undeformed conformation.

This motivates a phenomenological description of the capsid material which is based on the theory of thin plates. Here, the full three-dimensional strain energy reduces to a sum of a 2D in-plane stretching energy and a 2D bending energy [40]

$$E = E_e + E_b, \tag{1}$$

where

$$E_e = \mu \int dA\, u_j^i u_i^j + \frac{\lambda}{2} \int dA (u_i^i)^2 \tag{2}$$

and

$$E_b = 2\kappa_b \int dA\, H^2 + \kappa_g \int dA\, K. \tag{3}$$

Here, u_{ij} is the 2D strain tensor, K the Gaussian, and H the mean curvature. These quantities are completely determined by the first and second fundamental form [41]

$$2u_{ij} = g'_{ij} - g_{ij}, \tag{4}$$

where g'_{ij} is the metric of the deformed and g_{ij} that of the undeformed capsid. Thus, all energies are measured relative to the undeformed conformation. The mean curvature is given by the trace of the second fundamental form $2H=-b_i^i$, while the Gaussian curvature $K=\det(b_{ij})$ (for a more detailed explanation, see, e.g., Ref. [42]). Note that in Eq. (3) we do not take a spontaneous curvature into account since we assume that the capsomers prefer a planar conformation.

According to Gauss-Bonnet the surface integral of K is a topological invariant [41]. Thus, for the fixed surface topologies considered here it is a constant of integration which can be neglected in Eq. (3).

The 2D Lamé coefficients appearing in Eq. (2) are related to the 3D Young's modulus Y, 3D Poisson ratio σ, and shell thickness s via [40]

$$\lambda = \frac{\sigma}{1-\sigma^2} Ys \tag{5}$$

and

$$\mu = \frac{1}{2(1+\sigma)} Ys. \tag{6}$$

Typically σ lies in the range between 0.2 and 0.5 [43,44]. Triangular networks of springs have $\sigma=1/3$ and are thus suitable to describe the 2D limit of a wide range of materials [45]. The 2D Young's modulus κ_e is given by

$$\kappa_e = \frac{4\mu(\mu+\lambda)}{2\mu+\lambda} = Ys, \tag{7}$$

while the 2D bending modulus is given by

$$\kappa_b = \frac{Ys^3}{12(1-\sigma^2)}. \tag{8}$$

Here and in the following we set $\sigma=1/3$. As mentioned in the Introduction, the dimensionless Föppl–von Kármán number γ [24] is a convenient measure for the ratio between elastic and bending energy contributions,

$$\gamma \equiv R^2 \frac{\kappa_e}{\kappa_b} \approx 11 \left(\frac{R}{s}\right)^2. \tag{9}$$

Here, R is a typical length of the system, in the following chosen to be the radius of the shell.

The analogy between 2D elasticity and the elasticity of triangular networks makes them ideal to represent thin shells. Moreover, viral capsids themselves resemble such triangulated networks. In particular, 12 pentamers are required to complete the surface to a spherical shape. They can have large impact on the elastic behavior of the shell as a whole. As pointed out in Ref. [24] the Föppl–von-Kármán number governs the transition from the continuous shell regime to the regime, where the influence of these disclinations becomes predominant. More precisely, above a buckling threshold $\gamma_b \approx 154$ the pentamers form rigid cones, giving the viral shell a faceted icosahedral shape.

In the next section, we give qualitative results for the elasticity of shells based on a scaling analysis. A linear regime for small deformations and a nonlinear regime for larger deformations are identified that are separated by a shape transition. In Sec. II C we present analytical results for the linear regime including some predictions about the rupture behavior. The nonlinear regime and strongly buckled shells are investigated numerically. In Secs. III and IV we outline the foundations of our numerical analysis and present results on various aspects of shell stability.

B. Scaling analysis

For FvK numbers below the buckling threshold ($\gamma < \gamma_b$) spherical capsids can in good approximation be described as continuous 2D shells with no topological defects. On a qualitative level, their elastic properties can already be understood within the scaling analysis given here (which is based on Ref. [40]). Two regimes have to be distinguished: (i) a linear regime where small deformation forces lead to a linear response of the shell, and (ii) a nonlinear regime where above a critical force the mean curvature of the indented region abruptly changes sign.

1. Linear regime

Under small load the shell is flattened in an area of order d^2 (see Fig. 1). The indentation depth in this case is

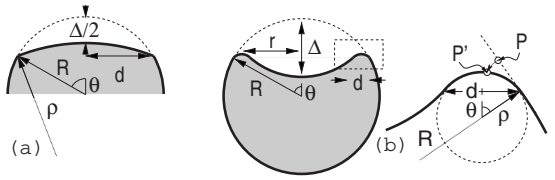

FIG. 1. (a) For small indentation the spherical shell with radius R is flattened under axial point load in a region of radius d and radius of curvature ρ. In the deformation region the meridians (dashed arc) are compressed. In this regime, the shell shape has an up-down symmetry since the reaction to the applied force acts at the point of contact with the supporting substrate. (b) At a critical indentation $\Delta_r \sim \gamma^{-1/2}R$ the shell undergoes a shape inversion. The deformation energy is mainly concentrated in a highly bent ring of radius r and width d. Again, ρ denotes the radius of curvature in the deformed area. Point P is moved to position P' which amounts to a compression of circles of latitude. Here, up-down symmetry is broken.

$$\frac{\Delta}{2} = R(1-\cos\theta) - \rho(1-\cos\theta') \approx \frac{1}{2}(R\theta^2 - \rho\theta'^2), \tag{10}$$

where we assume that the diameter of the deformed area is small, i.e., $\theta \ll 1$. The radius of the flattened region in this approximation is given by

$$d \approx \rho\theta' \approx R\theta. \tag{11}$$

The mean curvature in the deformed region is then given by

$$H \approx \frac{1}{\rho} \approx \frac{1}{R} - \frac{\Delta}{d^2}. \tag{12}$$

The change in Helfrich bending energy is of the order

$$E_b \approx 4\pi\kappa_b d^2\left(\frac{1}{\rho^2} - \frac{1}{R^2}\right) = 8\pi\kappa_b\left(\frac{1}{2}\frac{\Delta^2}{d^2} - \frac{\Delta}{R}\right). \tag{13}$$

In the last two equations it has been assumed that the mean curvature is constant on the deformed area (with surface area πd^2). The other factor 2 accounts for the up-down symmetry. In Eq. (13) we have neglected contributions from the edges of the flattened region giving rise to bending energies lower than that of the undeformed (spherical) reference state. This artifact of our approximation, however, does not affect the results of our scaling analysis since the force-distance relation [see Eq. (26)] is independent of the bending energy contributions linear in Δ.

The strain associated with the compression of meridians is

$$u \approx 1 - \cos\theta \approx \theta^2/2 \approx \frac{\Delta}{2R}. \tag{14}$$

For the in-plane elastic energy one has

$$E_e \approx 2\pi d^2\kappa_e u^2 = \frac{\pi}{2}\kappa_e\left(\frac{\Delta}{R}\right)^2 d^2. \tag{15}$$

The size d of the flattened area is set by mechanical equilibrium. Correspondingly, the total deformation energy must be minimal under variations in d leading to

$$d \approx 2^{3/4}R\gamma^{-1/4}, \tag{16}$$

and the total energy is

$$E \approx -8\pi\kappa_b\frac{\Delta}{R} + 2\sqrt{2}\pi\kappa_b\sqrt{\gamma}\left(\frac{\Delta}{R}\right)^2. \tag{17}$$

The force-distance law follows from

$$F = \frac{dE}{d\Delta} \approx -8\pi\frac{\kappa_b}{R} + 4\sqrt{2}\pi\sqrt{\gamma}\frac{\kappa_b}{R}\frac{\Delta}{R}. \tag{18}$$

The Δ-independent term appearing in Eq. (18) represents the force needed to bend the material without spontaneous curvature into the spherical shape. For materials with spontaneous curvature $C_0 = 1/R$ the last term is not present. In both cases, the force needed to deform the shell is only the Δ-dependent part of Eq. (18) and the force-distance relation reads

$$F \sim \frac{\kappa_b}{R}\sqrt{\gamma}\frac{\Delta}{R}. \tag{19}$$

In particular, in the linear regime the force scale is set by κ_b/R.

One should note that Eq. (19) holds only for sufficiently large γ since $d \ll R$ was assumed. Together with Eq. (16) this implies that our analysis is valid only for shells with an in-plane stiffness at least of the order of its bending stiffness.

2. Nonlinear regime

When the axial load exceeds a critical value, the curvature of the shell is spontaneously inverted inside a region of radius $r \sim R\theta$ as sketched in Fig. 1. Because the Helfrich energy depends only on the squared mean curvature inversion of the region does not cost any bending energy. However, there is an increase in bending energy coming from the small strip connecting the inverted with the noninverted parts. The main energetic contribution arises from this small strip of width d, where the shell is highly bent, see Fig. 1. The indentation depth is of the order of

$$\Delta \sim R(1-\cos\theta) \sim R\theta^2 \sim \frac{r^2}{R}, \tag{20}$$

and the radius r of the inversion is fixed by R and Δ. The only remaining parameter is the width d of the rim. For the radius of curvature in the bent zone ρ one has $d \sim \rho\theta \sim \rho\sqrt{\Delta/R}$ (see Fig. 1), and the bending energy is of order

$$E_b \sim \kappa_b rd\frac{1}{\rho^2} = \kappa_b\frac{1}{d}\frac{\Delta^{3/2}}{R^{1/2}}, \tag{21}$$

where the factor rd is coming from the area of the bent rim. The change in the in-plane elastic energy is dominated by the deformation along the circles of latitude. Their radii change by $\sim d\theta^2$ and the relative compression is

$$u \sim \frac{d\theta^2}{r} \sim \frac{rd}{R^2}. \tag{22}$$

The change in elastic energy caused by the in-plane deformation is given by

$$E_e \sim \kappa_e r d \left(\frac{rd}{R^2}\right)^2 = \kappa_e \frac{d^3}{R^{5/2}} \Delta^{3/2}. \tag{23}$$

In mechanical equilibrium the width of the deflected rim becomes

$$d \sim R^{1/2} \left(\frac{\kappa_b}{\kappa_e}\right)^{1/4}, \tag{24}$$

and the total deformation energy is

$$E \sim \Delta^{3/2} \frac{\kappa_e^{1/4} \kappa_b^{3/4}}{R}. \tag{25}$$

In this regime, the force-distance law is no longer that of a Hooke spring but rather has square root dependence on Δ,

$$F \sim \frac{\kappa_b}{R} \gamma^{1/4} \left(\frac{\Delta}{R}\right)^{1/2}. \tag{26}$$

This picture is valid only if the width of the rim does not exceed its radius. Hence, one expects the inversion transition to take place when $r \sim d$. According to Eqs. (20) and (24) the corresponding critical indentation is given by

$$\Delta_{\text{inv}} \sim R \gamma^{-1/2}. \tag{27}$$

Because of Eqs. (7) and (8), $R/\gamma^{1/2} \sim s$, and from Eq. (27) one expects that the transition to the nonlinear behavior takes place when the displacement Δ becomes comparable to the shell thickness s. Equation (27) and the linear force-distance law (19) determine the critical inversion force

$$F_{\text{inv}} \sim \frac{\kappa_b}{R}. \tag{28}$$

The scaling of the rupture force with γ can now be deduced from the scaling of the local strain. To do so, we assume that the material fails at a fixed critical strain u_r. For the linear regime Eq. (14) implies for the critical indentation depths

$$\Delta_r \sim R. \tag{29}$$

Similarly, one obtains from Eqs. (22) and (24) for rupturing in the nonlinear regime

$$\Delta_r \sim R \gamma^{1/2}. \tag{30}$$

Whether the shell actually ruptures in the linear or nonlinear regime depends on the prefactors of the scaling relations for Δ_{inv} and Δ_r. However, in both cases the rupture force scales as

$$F_r \sim \frac{\kappa_b}{R} \gamma^{1/2}. \tag{31}$$

C. Shape equation

Next, we want to derive the shape equation for a spherical shell under external loading. To do so, we calculate the total energy of a deformed sphere parametrized by the surface vector

$$\boldsymbol{R}' = \boldsymbol{R} + \eta^i \boldsymbol{R}_i + \psi \boldsymbol{N}, \tag{32}$$

where $\boldsymbol{R} = R(\sin\theta\cos\varphi, \sin\theta\sin\varphi, \cos\theta)$ is the surface vector of the undeformed sphere. The tangential vectors are given by $\boldsymbol{R}_i \equiv \partial_i \boldsymbol{R} \equiv \partial \boldsymbol{R}/\partial x^i$ with $x^1 = \theta$, $x^2 = \varphi$, and

$$\boldsymbol{N} \equiv \frac{\boldsymbol{R}_1 \times \boldsymbol{R}_2}{\sqrt{g}} \tag{33}$$

is the unit normal of the surface. g is the determinant of the first fundamental form given by

$$g_{ij} = \boldsymbol{R}_i \cdot \boldsymbol{R}_j = R^2 \,\text{diag}(1, \sin^2\theta). \tag{34}$$

The deformation fields ψ and η^i in Eq. (32) are the components of the displacement vector in the local coordinate system spanned by $\boldsymbol{N}$ and $\boldsymbol{R}_i$.

For the following, it is convenient to decompose the tangential deformation field η^i into an irrotational and a solenoidal part,

$$\eta^i = g^{ij} \partial_j \chi + \epsilon^{ij} \partial_j \zeta, \tag{35}$$

where ϵ^{ij} is the antisymmetric tensor in two dimensions, which can be rewritten using the Kronecker symbol δ^i_j as

$$\epsilon^{ij} = \delta^i_1 \delta^j_2 - \delta^i_2 \delta^j_1. \tag{36}$$

Here, we are interested in the deformation induced by an axial force exerted at the north pole of the sphere (at $\theta = 0$) sitting on a planar substrate. To analyze this scenario analytically we have to restrict the analysis to the linear regime (before the inversion transition discussed in the last section). Then, the sphere has a single point of contact with the supporting substrate at $\theta = \pi$. Consequently, the reaction to the force applied at $\theta = 0$ is acting as a point force at $\theta = \pi$. Because the (slightly) indented sphere has a reflection symmetry with respect to the $\{\theta = \pi/2\}$ plane the normal displacements at the two poles are given by

$$\psi|_{\theta=0} = \psi|_{\theta=\pi} = -\frac{\Delta}{2}. \tag{37}$$

To determine the stationary shapes with surface vector Eq. (32) the displacement fields ψ, χ, and ζ have to be chosen such that the first variation of the deformation energy vanishes. For the variations of the normal displacement field $\psi \to \psi + \delta\psi$ the constraint given by Eq. (37) has to be satisfied, implying

$$\delta\psi|_{\theta=0} = \delta\psi|_{\theta=\pi} = 0. \tag{38}$$

The deformations induced by the radial point force lead to deformation with axial symmetry and there is no φ dependence of the displacement fields. From Eq. (35) and the diagonal structure of g_{ij} we conclude that

$$\eta^\theta = g^{\theta\theta} \partial_\theta \chi = \frac{1}{R^2} \partial_\theta \chi. \tag{39}$$

Furthermore η^φ must vanish for symmetry reasons, i.e.,

$$\eta^\varphi = -\partial_\theta \zeta = 0. \tag{40}$$

Thus, the solenoidal part ζ does not contribute to the total energy.

Next, the energy of the deformed sphere can be calculated by expanding (1) in the deformation fields ψ and χ. The calculation is somewhat tedious since it involves the calculation of the metric g'_{ij} and the second fundamental form b'_{ij} of the deformed sphere, where

$$b'_{ij} \equiv \boldsymbol{R}'_{ij} \cdot \boldsymbol{N}', \tag{41}$$

where $\boldsymbol{N}'$ is the normal vector of the deformed surface.

One finally obtains in second order

$$E_b = \frac{1}{2}\frac{\kappa_b}{R^2}\int dS(4 + 2\psi\psi^i_i + R^2\psi\psi^{ij}_{ij}) + O((\psi)^\mu(\chi)^\nu), \tag{42}$$

$$E_e = \frac{3}{16}\frac{\kappa_e}{R^2}\int dS\left(\chi\chi^i_i + \frac{3}{2}R^2\chi\chi^{ij}_{ij} + 4R\chi\psi^i_i + 4\psi^2\right) + O((\psi)^\mu(\chi)^\nu), \tag{43}$$

where $\mu+\nu=3$ and dS denotes the area element of the undeformed sphere. The indices of the scalar quantities χ and ψ denote covariant derivatives, i.e., $\psi_{ij} \equiv D_j\psi_i$. The covariant derivative of a contravariant vector a_i is defined by

$$D_j a_i = \partial_j a_i - a_k\Gamma^k_{ij}. \tag{44}$$

Likewise, for a covariant vector a^i one has

$$D_j a^i = \partial_j a^i + a^k\Gamma^i_{kj}. \tag{45}$$

Here, the Γ^i_{jk} are the Christoffel symbols of the second kind [41]. In deriving Eqs. (42) and (43) we have taken into account that covariant derivatives do not commute, i.e.,

$$[D_i, D_j]a_l = a_k R^k_{lji}, \tag{46}$$

where R^l_{kji} is the Riemann curvature tensor [41]. For a more detailed discussion in a similar context see, e.g., Ref. [42].

The easiest way to satisfy the constraints given by Eq. (37) on ψ is to expand the deformation fields ψ and χ in spherical harmonics Y_{lm} [46]. As mentioned above, we restrict the analysis here to small deformations for which the deformed sphere has an up-down symmetry. Since additionally the deformation fields do not depend on φ, only the Y_{lm} with even l and $m=0$ contribute, i.e.,

$$\psi = R\sum_{l=0}^{\infty} A_l Y_{2l,0} \tag{47}$$

and

$$\chi = R^2\sum_{l=0}^{\infty} B_l Y_{2l,0}. \tag{48}$$

Upon choosing

$$A_0 = -\sqrt{\pi}\frac{\Delta}{R} - \sum_{l=1}^{\infty}\sqrt{4l+1}A_l, \tag{49}$$

the constraint (37) is satisfied and the total energy becomes

$$E = \kappa_b\sum_{l=0}^{\infty}\left(2l^2(2l+1)^2 - 2l(2l+1) + \frac{3}{2}\gamma\right)A_l^2 + \frac{3}{4}\gamma[3l^2(2l+1)^2 - l(2l+1)]B_l^2 - 3\gamma l(2l+1)A_lB_l \equiv \kappa_b\sum_{l=0}^{\infty}\alpha_l A_l^2 + \beta_l B_l^2 + \delta_l A_l B_l. \tag{50}$$

As expected, there is no contribution coming from B_0 (since $\beta_0=\gamma_0=0$) since the energy depends only on the derivative of χ. By inserting relation (49) and varying the expansion coefficients as $A_l \to A_l + a_l$, $B_l \to B_l + b_l$, one obtains for the first variation of the energy

$$\delta E = \kappa_b\sum_{l=1}^{\infty} a_l(2A_l\alpha_l - 2\alpha_0\sqrt{4l+1}A_0 + \delta_l B_l) + b_l(\delta_l A_l + 2\beta_l B_l). \tag{51}$$

In mechanical equilibrium the deformed sphere obeys the shape equation $\delta E=0$, implying

$$A_l = \frac{K_0}{K_l}\sqrt{4l+1}A_0 \tag{52}$$

and

$$B_l = -\frac{\delta_l}{2\beta_l}A_l, \tag{53}$$

where

$$K_l \equiv 2\alpha_l - \frac{\delta_l^2}{2\beta_l} \tag{54}$$

and

$$K_0 = 2\alpha_0. \tag{55}$$

With Eqs. (49) and (52) the total energy simplifies to

$$E = \kappa_b\frac{\pi}{2}\left(\frac{\Delta}{R}\right)^2\left(\sum_{l=0}^{\infty}\frac{4l+1}{K_l}\right)^{-1}. \tag{56}$$

The linear spring constant for a radial point force is found from

$$k \equiv -\frac{1}{\Delta}\frac{\partial E}{\partial \Delta} = -\frac{\kappa_b}{R^2}\pi\left(\sum_{l=0}^{\infty}\frac{4l+1}{K_l}\right)^{-1}. \tag{57}$$

The infinite sum appearing in Eq. (57) can (with the help of MATHEMATICA [47]) be expressed as

$$\sum_{l=0}^{\infty}\frac{4l+1}{K_l} = \frac{\ln 16 - 4 + 2\Gamma}{8+3\gamma} + \frac{1}{2}\sum_i \frac{-\Psi(-x_i) + 3\Psi(-x_i)x_i + 6\Psi(-x_i)x_i^2}{-2+3\gamma+10x_i+20x_i^2}, \tag{58}$$

where $\Gamma \simeq 0.577\,216$ is Euler's constant and $\Psi(x) \equiv d\ln\Gamma(x)/dx$ denotes the logarithmic derivative of the

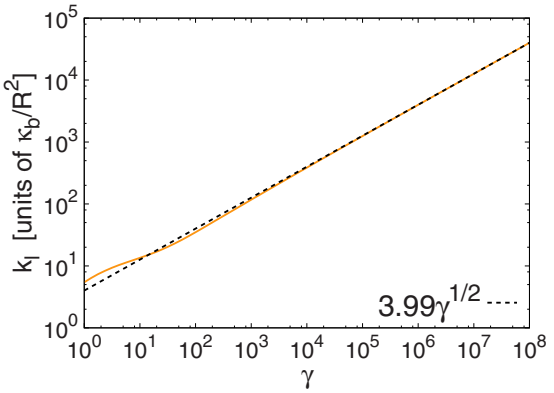

FIG. 2. (Color online) Analytically calculated spring constant k_l as a function of γ for a supported elastic sphere indented at $\theta=0$ by a radial point force. For Föppl–von Kármán numbers γ below 10 the spring constant deviates noticeably from the $\gamma^{1/2}$ behavior. Asymptotically the curve fits $k_l=3.99\sqrt{\gamma}\kappa_b/R^2$ (fit was made for $\gamma=10^3,\ldots,10^8$).

Gamma function [46]. The x_i are the zeros of the fourth-order polynomial

$$P(x) = -3\gamma - 4x + 4x^2 + 48x^3 + 48x^4. \tag{59}$$

With the explicit representation (58) the sum in Eq. (57) can be numerically evaluated without having to truncate it at some large (but finite) l. The only limiting factor is thus the numerical precision with which the zeros of the polynomial (59) can be determined numerically.

The spring constant determined in this way is plotted as a function of the Föppl–von Kármán number in Fig. 2. Asymptotically the curve agrees well with the square root behavior expected from the scaling analysis given above:

$$k = 3.99\frac{\kappa_b}{R^2}\sqrt{\gamma}. \tag{60}$$

This relation was found by Reissner [48] in the thin shell limit of a 3D elastic theory. However, Eq. (9) implies that the thin shell approximation is equivalent to $\gamma\to\infty$. The considerable deviations from the square-root law occurring for smaller γ are captured only by our more general expression Eq. (57).

D. Comparison with scaling analysis

Our analytical approach is so far limited to the linear regime of small indentations which do not lead to inversion of the local mean curvature at the point of loading. However, it can be extended to make predictions about rupture and the onset of the inversion transition.

The γ dependence of this critical indentation can be found analytically from the condition

$$H(\theta,\Delta_{\text{inv}}(\gamma),\gamma)|_{\theta=0} = 0, \tag{61}$$

where

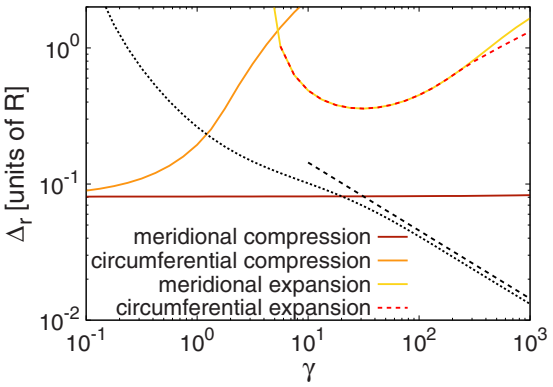

FIG. 3. (Color online) γ dependence of the critical indentation for various types of rupturing. It is assumed that rupturing occurs at a relative bond length change of 4.5% (see Sec. IV D). The compression of meridians is responsible for rupture at small Δ_r. The critical indentation Δ_r is independent of γ, in agreement with the scaling picture. The dotted line shows the γ dependence of the inversion transition. For $\gamma\leqslant 20$ rupturing occurs before inversion, i.e., in the linear regime. The black dashed line is a fit to $\gamma^{-1/2}$.

$$H \equiv -\frac{1}{2}b_i^i \tag{62}$$

denotes the mean curvature. In Eq. (61) it is assumed that $H(\Delta)$ goes through zero continuously. In the linearized problem this is indeed the case, since here H is a linear function of the deformation. However, as will be shown later in Sec. IV, for large γ this transition becomes discontinuous.

The solution of Eq. (61) is plotted in Fig. 3 (black dotted line). For small γ the curve deviates from the expected $\gamma^{-1/2}$ behavior [see Eq. (27)], since the equilibrium configuration is dominated by the bending energy, which is scale invariant. The point force thus leads to a shape-invariant shrinking of the shell. One must also keep in mind that our analytical analysis is based on a linear expansion in the deformation and holds only for $\Delta^2\ll R^2$.

Using the analytical results for the deformation fields ψ and η, we can also determine the γ dependence of the rupture indentation Δ_r. The strain tensor u_{ij} has elements

$$u_{\theta\theta} = \psi \tag{63}$$

and

$$u_{\varphi\varphi} = \sin\theta(\eta^\theta\cos\theta + \psi\sin\theta). \tag{64}$$

For axial-symmetric loading the off-diagonal terms vanish. The strain tensor is closely related to the local change of the first fundamental form [see Eq. (4)] and we can express the relative length change in direction of the ith coordinate via

$$\delta_i \equiv \sqrt{1+2u_{ii}} - 1, \tag{65}$$

where $i=\theta,\varphi$. Then, at the rupturing indentation Δ_r the relative length change δ_i reaches a critical strain u_r

$$\max_{\theta\in[0,\pi]}[\pm\delta_i(\theta,\Delta_r)] = u_r. \tag{66}$$

Here, $(+)$ corresponds to critical expansion and $(-)$ to critical compression. Furthermore, $i=\theta$ corresponds to meridi-

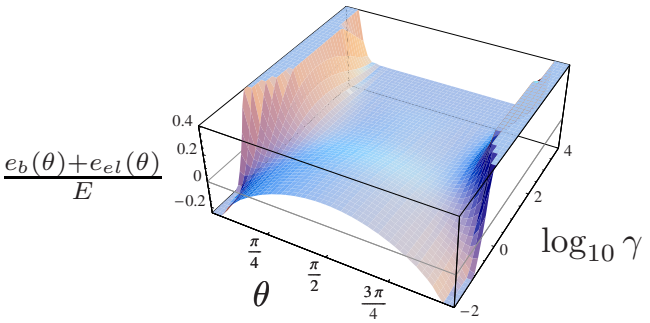

FIG. 4. (Color online) Distribution of deformation energy along the θ coordinate as a function of the Föppl–von Kármán number γ. For the evaluation of the energy density ψ and η have been expanded in spherical harmonics up to $Y_{40,0}$. For $\gamma<1$ the deformation energy concentrates along the equator.

onal and $i=\varphi$ to circumferential in-plane deformation. The four different scenarios are compared in Fig. 3. In accordance with the scaling analysis of Sect. II B the shell ruptures most likely due to meridonal compression at a critical indentation Δ_r which is independent of γ. As mentioned, the analytical results are valid only in the limit $\Delta^2 \ll R^2$ which is satisfied for meridonal compression. Δ_r exceeds the inversion threshold only above $\gamma \simeq 20$ (see Fig. 3). Our analytical approach does not hold in this regime.

The derivation of the scaling results is based on the assumption that only a small region around the poles are deformed. With our analytical results we can check the validity of this assumption. For this purpose we plot the (normalized) density of deformation energy $e_{\mathrm{el}}+e_b$ as function of θ and γ (see Fig. 4). This density is given by the integrand of the total energy defined in Eqs. (1)–(3). The normalization constant

$$E = \int_0^\pi d\theta [e_b(\theta) + e_{\mathrm{el}}(\theta)]. \tag{67}$$

The flattening of the polar region leads to a local decrease in bending energy. In case of dominating bending energy, i.e., $\gamma<1$, the deformation energy concentrates around the equator, contradicting our assumptions. For higher γ, however, the flattening leads to an increase in the density of the total deformation energy at the poles.

III. NUMERICAL INVESTIGATION

So far, we have used in our analysis a continuum description of the shell without defects. As explained, our results cannot be expected to hold in the regime above the buckling threshold. Many interesting phenomena are thus analytically intractable. However, numerical simulations of capsids under external loading give valuable insights into their elastic and inelastic behavior [25].

In our simulations, the viral capsids are represented by an icosadeltahedron with appropriate Caspar-Klug numbers. In particular, we have implemented capsids with triangulations $T=169$ and 1183 corresponding to the PBCV1 and mimivirus capsids, respectively. In addition to these specific geometries we have also studied the triangulation $T=49$ [which allows for two distinct (h,k) representations] to analyze more general aspects of chiral capsid design. To our knowledge a virus with this particular T has not yet been discovered.

In our simulations, the centers of the capsomers are represented by vertices connected to each other with harmonic springs with spring constants $\tilde{\kappa}_e$. The associated harmonic potential models the elastic (stretching) part of the deformation energy

$$E_e = \frac{\tilde{\kappa}_e}{2} \sum_{\langle i,j \rangle} (l - |\boldsymbol{r}_i - \boldsymbol{r}_j|)^2, \tag{68}$$

where $\boldsymbol{r}_i$ denotes the position of the ith vertex and l is the preferred vertex distance. The sum extends over all nearest neighbor pairs $\langle i,j \rangle$. The 2D Young's modulus of the elastic network is related to the spring constant $\tilde{\kappa}_e$ via $\kappa_e = 2\tilde{\kappa}_e/\sqrt{3}$ [37].

The bending energy can be expressed in terms of the normal vectors of the facets of the triangulated surface. This can be done in different ways (see Appendix A). We chose the method described in Ref. [36] throughout, since it gives the most reliable results even for strong deformations. In this discretization scheme the bending energy is given by

$$E_b = 2\kappa_b \sum_i \frac{C_i^2}{A_i}, \tag{69}$$

where the sum extends over all edges. A_i is the network area of the ith edge, i.e., one-third of the area of the two adjacent triangles. The mean curvature of the ith edge is given by [36]

$$C_i = \frac{\boldsymbol{k} \cdot (\boldsymbol{n}_1 \times \boldsymbol{n}_2)}{|\boldsymbol{n}_1||\boldsymbol{n}_2| + \boldsymbol{n}_1 \cdot \boldsymbol{n}_2}. \tag{70}$$

Here, $\boldsymbol{n}_1$ ($\boldsymbol{n}_2$) are the non-normalized normal vectors of the adjoint triangles left (right) of the ith edge and $\boldsymbol{k}$ is its non-normalized direction vector. The discretization Eq. (70) is an approximation of the Helfrich Hamiltonian [49] for small dihedral angles between $\boldsymbol{n}_1$ and $\mathbf{n}_2$.

The shape of minimal energy is then found by minimizing the total energy $E=E_e+E_b$ using a conjugate gradient algorithm [50]. To do so, we have constructed a regular icosadeltahedron with the desired quasisymmetry. Initially, we have set $\kappa_e \equiv R\gamma^{1/2}$ and $\kappa_b \equiv 1/\kappa_e$ with $R \equiv (A/4\pi)^{1/2}$. Here, A is the surface of the shell, i.e., the sum of the areas of all facets. With these values, the total energy was numerically minimized. Then, with the new surface area, the values R, κ_e, and κ_b were recalculated and the total energy was minimized again. This procedure was repeated until R converged.

To simulate the indentation experiments vertices i at the point of loading were moved away from their equilibrium position $\boldsymbol{r}_i$. We thus work in an ensemble of prescribed indentation $\boldsymbol{\Delta}$ rather than in an ensemble of applied force. Generally, all vertices (except the indented vertex i) are free to move; they are only constrained to lie above a (virtual) plane at $z=0$. The shape of the triangulated surface under these constraints is also found by minimizing the total energy.

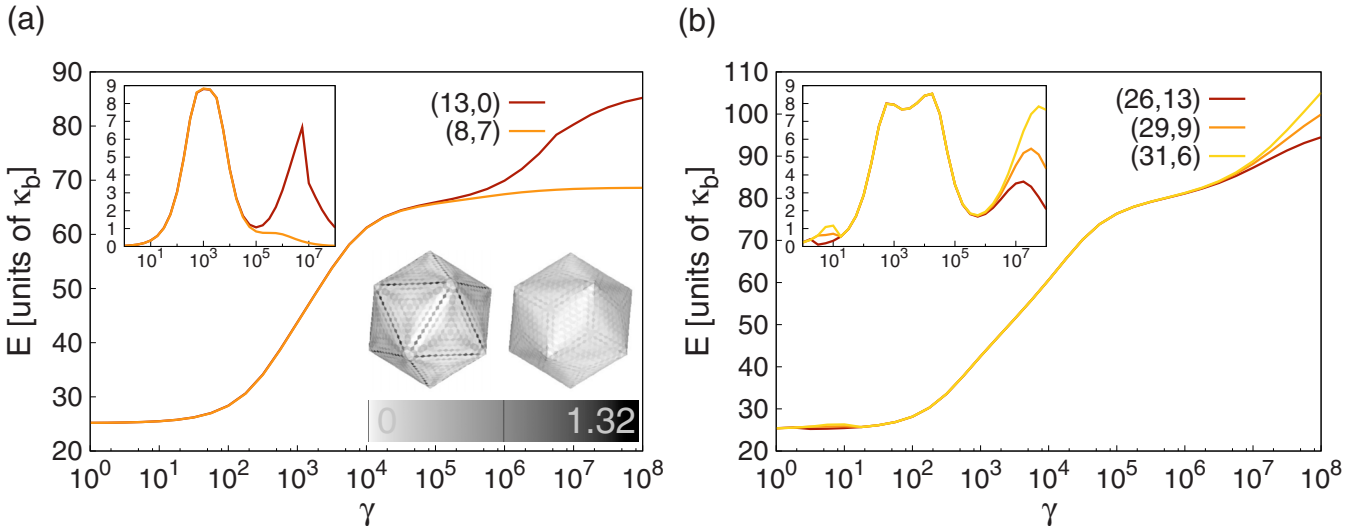

FIG. 5. (Color online) (a) Total energy of the different (h,k) realizations with triangulation $T=169$ corresponding to a PBCV1 capsid. Clearly, the chiral structure is favorable for FvK numbers $\gamma > 10^5$. The inset shows the in-plane elastic part of the total energy. The buckling transition is characterized by an increase in stretching energy leading to a pronounced peak at $\gamma \simeq 10^3$. Above $\gamma \simeq 10^5$ the nonchiral structure is more strongly stretched than the chiral one. The structures depicted on the lower right are the nonskew (left) and the skew capsid (right) at $\gamma = 10^6$. The distribution of in-plane elastic energy is shown on a common gray scale in units of $10^{-5}\kappa_b$. Dark areas represent strong stretching or compression. (b) Total energy for a $T=1183$ structure corresponding to a mimivirus capsid. Here, the (26, 13) structure is the most favorable one although noticeable differences become visible only above $\gamma \simeq 10^6$.

To generate force distance curves the buckled capsids were indented stepwise with a step width $\delta\Delta = R/250$. At each step the corresponding indentation force was determined using the relation

$$F = -\frac{\delta E}{\delta \Delta}, \tag{71}$$

where δE is the change of the deformation energy between two successive steps.

IV. NUMERICAL RESULTS

In this section numerical results on the stability of viral capsids are presented. First, we discuss skew shell designs under the energetic aspects. In the following sections we discuss elastic and inelastic properties of viral capsids. Here, our focus lies on the structural inhomogeneity of capsids and the influence of a skew viral design on shell elasticity. We complete the section with a discussion of capsid stability under large internal pressures. In particular, we analyze the influence of the pressure distribution which arises from the organized packing of DNA. We discuss both an ensemble with prescribed pressure and prescribed volume.

A. Chiral viruses

Most spherical viral capsids have icosadeltahedral symmetry with a certain skewness $(h,k \neq 0)$ and even chirality $(h \neq k)$. This handedness may arise from an inherent handedness of the capsid proteins [51]. Additionally, as we show now with our numerical analysis a skew design is also favorable for energetic reasons. The handedness of the capsomers determines whether the capsid is left or right handed.

Figure 5 gives an example where the total energy of the two realizations (8,7) and (13,0) of PBCV1 viral capsids (with $T=169$) [15] are compared. As can be seen from the insets in Fig. 5, the edges of the icosahedral superstructure are stretched more in the nonchiral capsid than in the chiral one. For $\gamma > 10^5$ the energy difference becomes dominant such that the (8,7) structure is favorable. Similar results are obtained for CIV capsids with $T=147$ (data not shown). Here, the (7,7) structure has lower elastic energy than the (11,2) structure for $\gamma > 10^5$. Like PBCV1, the CIV capsid has $\gamma \simeq 10^3$ [16]. Although, there is no significant energetic difference between chiral and nonchiral structures at this FvK number, the wild type PBCV1 and CIV prefer the chiral structures, i.e. Caspar-Klug numbers which have lowest energy for large γ.

More generally, these findings indicate that those icosadeltahedra are energetically preferred (for large γ), which have the smallest difference $|h-k|$. This can be justified as follows. Buckling is associated with a large strain along the icosahedral edges. For an (h,k) structure this strain is distributed among the $h+k$ bonds connecting the pentamers. Thus, the larger k the smaller the strain per bond. Additionally, for $k \neq 0$ the strain can also be reduced by a change of the bond angles. Since stretching or compression of bonds contributes quadratically to the total energy via the elastic energy, the strain saving geometry has a much lower energy. This effect becomes more visible the higher the contribution of the stretching energy, i.e., the larger γ.

B. Spring constants

Next, we compare the mechanical response of capsids with different skewness to externally applied indentation

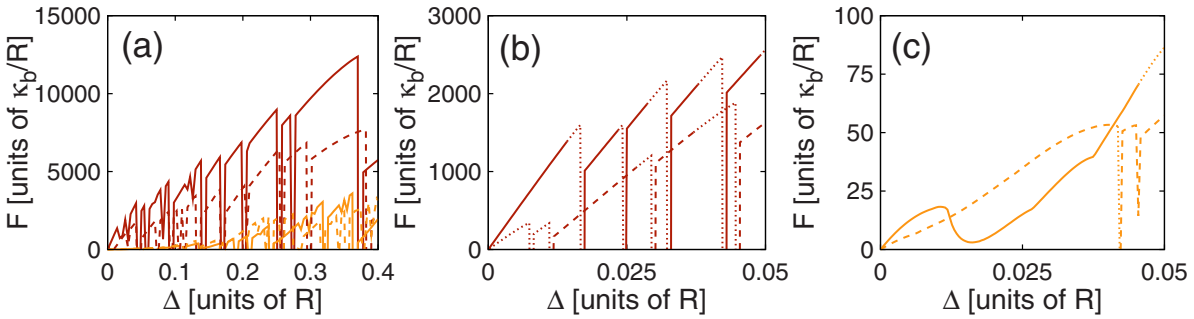

FIG. 6. (Color online) (a) Typical force distance curves for hexamers [orange (light gray) lines] and pentamers [red (dark gray) lines] for chiral (solid lines) and nonchiral (dashed lines) structures at $\gamma=10^6$. (b), (c) Detailed view of the elastic behavior of pentamers (b) and hexamers (c) for very small indentations. The dotted curves represent deformations of metastable conformations.

forces. From the scaling analysis of Sec. II B one expects that the capsids respond linearly to small forces. This regime is explored here for a $T=49$ structure in both the skew (5, 3) and nonskew (7, 0) design.

Viruses were indented radially by a distance Δ varying with step size $\delta\Delta=R/250$ as described above. Both hexamers and pentamers were displaced. The indented hexamers discussed here all lie in the center of the facet spanned by their three neighboring pentamers, i.e., they are the points of threefold icosahedral symmetry. For small indentations the observed force-distance curves are linear with a spring constant defined via

$$k_l = \frac{F}{\Delta}. \tag{72}$$

Figure 6 shows typical force distance curves for $\gamma=10^6$. As was already shown in Ref. [25] the force-distance curves at such high FvK numbers are characterized by discontinuous jumps. The sudden drops in the restoring force represent transitions between stable indented configurations. The transitions can be discontinuous accompanied by metastable states which have higher deformation energy than stronger deformed conformations.[1] In Figs. 6(b) and 6(c) these states are plotted as dotted lines. Figure 6 also shows that metastable states are encountered much more frequently when pentamers are probed.

The analysis of force distance curves for γ ranging from 10 to 10^8 is summarized in Fig. 7. Below $\gamma\simeq10^3$ the spring constants of both pentamers and hexamers follow nicely the analytical curve. In general, for larger FvK numbers pentamers become stiffer with a spring constant which roughly scales as γ^1. Hexamers become softer. As can be seen from Fig. 7 the (5, 3) and (7, 0) structures have identical elastic response up to $\gamma\simeq10^5$. For larger γ the skew capsid has a larger spring constant than the nonskew structure. This effect is much more pronounced when the capsid is pushed on its hexamers. Here, the spring constants scale approximately as γ^1 ($\gamma^{1/2}$) for the skew (nonskew) capsids. For loading on pentamers there is hardly any difference in the elastic response.

[1]For $\gamma<100$ the transition is continuous; for $\gamma>10\,000$ it is discontinuous.

C. Material properties

With the aid of numerical simulations it is possible to extract precise material parameters of experimentally investigated viruses. To do so, we simulated indentation experiments under the conditions corresponding to the SFM experiments on the phages $\phi29$ [5], λ [52], the plant virus cowpea chlorotic mottle virus (CCMV) [9], and the animal viruses minute virus of mice (MVM) [10] and murine leukemia virus (MLV) [8]. Their FvK numbers can be estimated from their geometry via the relation Eq. (9). Note that this relation is based on the thin shell approximation. For MLV the validity of the thin shell limit is at least arguable.

The shapes of the viral capsids of interest have been quantitatively characterized by cryo-electron-microscopy (EM) and x-ray studies [19,53–56]. For example, phage $\phi29$ has an average equatorial radius $R\simeq21$ nm and a shell thickness of $s\simeq1.6$ nm. As its FvK number $\gamma\simeq2000$ indicates, the shape of $\phi29$ is noticeably buckled. For CCMV the corre-

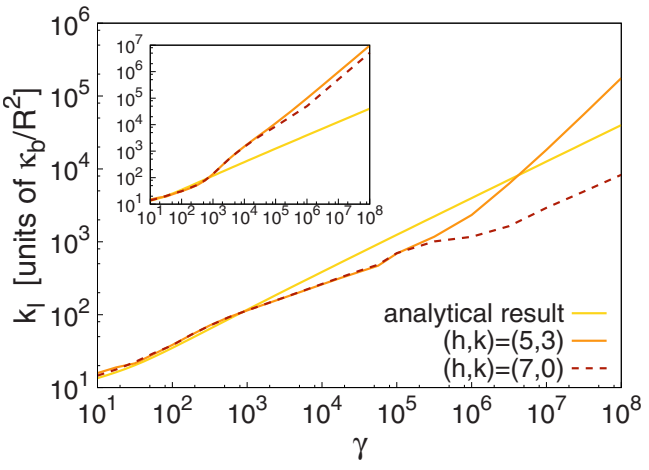

FIG. 7. (Color online) Spring constants of hexamers and pentamers (inset) as function of the FvK number γ. Below $\gamma\simeq10^3$ the linear elasticity of spherical capsids is well described by the analytical results of the homogeneous shell approximation. Above $\gamma\simeq10^3$ pentamers become stiffer and hexamers softer. Pentamers show a $k_l\sim\gamma^1$ scaling. Above $\gamma\simeq10^5$ the linear spring constants of hexamers are considerably softer for nonchiral shells than for chiral ones. They show a $k_l\sim\gamma^1$ ($k_l\sim\gamma^{1/2}$) scaling in the skew (nonskew) case. As the inset shows, the difference is less pronounced for pentamers.

TABLE II. Estimated material properties of viruses, whose elasticity has been probed in SFM experiments. The values for R, s, and k_l are taken from the references given in the text. γ has been calculated from R and s. Here, s is the shell thickness and R the mean shell radius. The elasticity of filled capsids is discussed in Sec. IV E. The tolerance of the bending stiffness of CCMV arises from the numerically observed bimodality of the spring constant distribution.

	R (nm)	s (nm)	γ	k_l (N/M)	κ_b/R^2 (mN/m)	Y (GPa)
ϕ29	21	1.6	1778	0.16	1.14	1.3
λ	31.5	2.9	1300			
Empty				0.13	1.02	0.41
Filled				0.23	1.01	0.41
CCMV	12.3	2.3	310			
Empty				0.15	2.4 ± 0.2	0.24 ± 0.02
Filled				0.20	3.3 ± 0.5	0.33 ± 0.05
MVM	14.6	5.4	80	0.56	16.3	0.24
MLV						
Immature	435	370	15	0.33	18.3	0.0007
Mature	570	100	360	0.13	2.0 ± 0.4	0.007

sponding values are $R \simeq 12$ nm and $s \simeq 2.5$ nm. Thus, $\gamma \simeq 300$ and CCMV is slightly buckled. The estimated FvK numbers for all investigated viruses are summarized in Table II.

For ϕ29 the estimate of its FvK number can be refined using the available experimental information about the bimodal spring constant distribution. By using the FvK number γ as fit parameter for the measured bimodality ratio $k_l^{(5)}/k_l^{(6)} \simeq 1.88$ one finds $\gamma \simeq 1778$, in good agreement with the value estimated above from the geometrical parameters [19].

Then, $\kappa_b/R^2 \simeq 1.14$ mN/m can be extracted from the (dimensionless) numerical spring constant $k_n \equiv k_l R^2/\kappa_b$ for the softest experimentally measured value of $k_l^{(6)} = 0.16$ N/m (with corresponding $k_l^{(5)} = 0.296$ N/m) [5]. From the bending stiffness and the shell geometry the 3D Young's modulus $Y \simeq 1.3$ GPa can be calculated via Eq. (8). This value is in agreement with earlier estimates based on finite element methods [5]. The estimated elastic moduli of all investigated viruses are summarized in Table II. The values for filled viruses were obtained from a numerical scheme introduced in Sec. IV E.

Apart from ϕ29, for none of these capsids has a bimodality been reported. As can be seen from Table II, the phages λ and ϕ29 have estimated γ values far above the buckling threshold, while the animal and plant viruses have FvK numbers below or slightly above γ_b. Therefore, one would not expect a noticeable bimodal spring constant distribution for CCMV, MLV, and MVM.

In contrast, phage λ is very strongly buckled. In cryoEM images it appears as a sharply edged icosahedron (see Ref. [54]). However, the measurement in Ref. [52] were performed on phages with intact tails. One end of these rather long tails is incorporated into the capsid in place of one pentamer. Therefore, these capsids always expose their icosahedral faces to the SFM tip. This explains the absence of a second spring constant for phage λ in Ref. [52].

For empty CCMV the bimodality cannot be resolved experimentally ($k_l = 0.15 \pm 0.01$ N/m [9]). Numerically, we find a slightly higher spring constant for hexamers, $k_l^{(6)} = 0.17$ N/m and $k_l^{(5)} = 0.12$ N/m. Here, we extract $\kappa_b/R^2 \simeq 2.4 \pm 0.2$ mN/m and $\kappa_b/R \simeq 29 \pm 2$ pN from the numerical data.

The bulk elastic moduli for MLV are remarkably small. In contrast to the other investigated capsids, MLV is an enveloped virus [56]. Its shell has a by far more complex composition than the capsids discussed in the Introduction, and in particular lacks icosahedral symmetry. Moreover, the envelope is typically a lipid membrane with a much softer bulk elasticity compared to shells that are entirely composed of tightly bound capsid proteins. The bending stiffness of the viral capsid of MLV changes drastically during maturation. Accordingly, the 3D bulk Young's modulus increases tenfold while still being very small (see Table II). One must note, however, that the suitability of the thin shell approximation is arguable in this case, since the ratio R/s is close to 1.

D. Rupture

As a next step we have analyzed numerically the rupture of shells. Rupture is assumed to occur when a bond reaches a critical strain u_r [see Eq. (66)]. To get an estimate for the numerical value of u_r we have simulated a SFM experiment with parameters chosen to mimic phage ϕ29 [25]. Analyzing the structure at the experimentally determined rupture force reported in Ref. [5] yields a critical strain of $u_r = 4.5\%$. However, other viruses might have different critical strains due to different chemical composition.

Numerically, the capsid was indented until for some bond the critical length change of 4.5% was reached. At this critical indentation Δ_r, the rupture force F_r was determined using Eq. (71).

Figure 8(a) shows the rupture force as a function of γ. There is no significant difference between the rupture behaviors of skew and nonskew structures. For $\gamma < 10^4$, the rupture force scales as $\gamma^{1/2}$, in agreement with the scaling arguments. As discussed above for $\gamma < 10^2$, scaling arguments do not

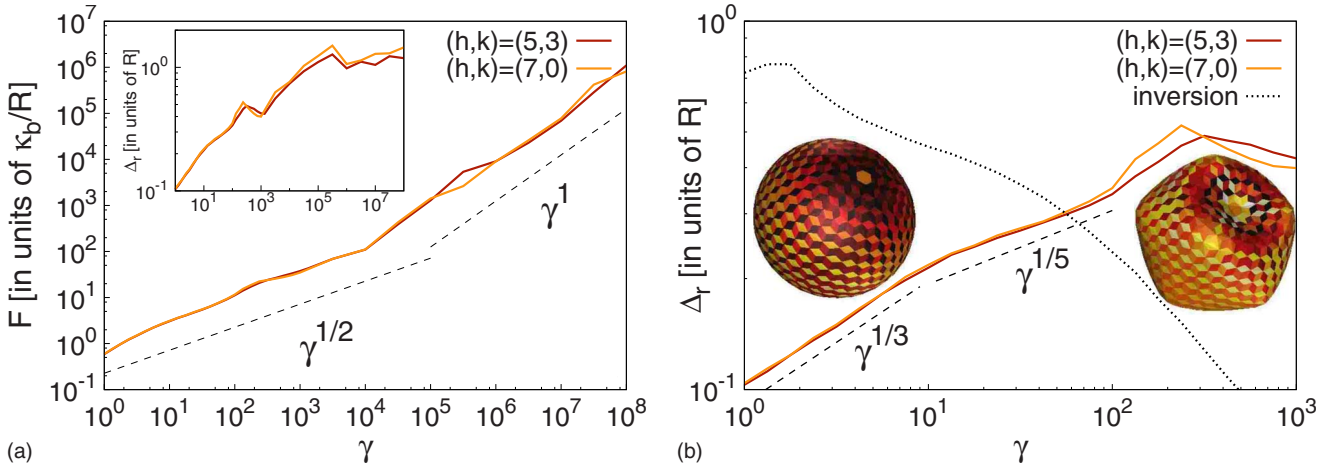

FIG. 8. (Color online) (a) Rupture force of hexamers as function of γ for a nonchiral (7, 0) and a chiral (5, 3) structure. For $\gamma < 10^4$ we observe a $\gamma^{1/2}$ scaling of the rupture force in agreement with thin shell theory. For $\gamma > 10^4$, rupture force scales as γ^1. (Inset) Rupture indentation for the same data. (b) Plot of the rupture indentation Δ_r as a function of γ. Numerically we observe a crossover from a $\gamma^{1/3}$ to a $\gamma^{1/5}$ scaling at $\gamma \approx 10$. The dotted line represents the numerically determined inversion threshold. Thus, rupturing occurs in the linear regime for $\gamma < 100$. The force distance curves for this γ range are indeed perfectly linear (data not shown). The insets show the strain distribution in a (5, 3) structure for $\gamma = 10$ (left) and 1000 (right) at the respective rupture indentations. Compressed (stretched) areas are colored in dark red [black] (yellow [light gray]).

apply. In this regime, we observe roughly a $\gamma^{2/3}$ scaling as already reported in Ref. [25].

The γ dependence of Δ_r is shown in the inset of Fig. 8(a). It differs strongly from the $\Delta_r \sim \gamma^0$ behavior expected from scaling arguments. As shown in Fig. 8(b) we observe a $\gamma^{1/3}$ scaling of the rupture indentation in this regime. In a regime between $\gamma = 10$ and γ_b we observe a $\gamma^{1/5}$ scaling. Figure 8(b) also shows that above $\gamma \simeq 70$ rupture already occurs in the nonlinear regime. The insets in Fig. 8(b) show the strain distribution in a (5, 3) structure for $\gamma = 10$ and 1000 at the respective rupture indentations.

As implicitly assumed in the above scaling analysis, meridians are compressed in the linear regime. Here, however, the strain extends over a large area for $\gamma < 100$, covering also pentamers further away from the point of loading. Therefore, the strain no longer distributes homogeneously as assumed by the continuum shell theory [see the left inset in Fig. 8(b)]. This might explain the deviations from the predicted $\Delta_r \sim \gamma^0$ scaling (cf. Fig. 3).

Instead of the expected $\Delta_r \sim \gamma^0$ scaling, we observe a sharp transition from a $\gamma^{1/3}$ to a $\gamma^{1/5}$ scaling at $\gamma \approx 10$ [see Fig. 8(b)]. This crossover in scaling might reflect the discrete distribution of disclinations. As Eq. (16) shows, the area over which the strain distributes scales as $\gamma^{-1/2}$. Thus, when γ becomes smaller, the strain extends over a larger area, finally including the next set of pentamers.

Above the inversion transition the strain is distributed concentrically around the point of loading, supporting the assumptions of the scaling arguments. However, for γ larger than the buckling threshold γ_b the scaling arguments break down due to the dominance of the disclinations.

In a typical SFM experiment the capsid is repeatedly pushed with the SFM tip [5]. Since the tip is moving along the surface, the stability is not probed at a single well-defined locus but rather at an ensemble of indentation sites. To mimic this experimental procedure we have also performed simulations of ensemble measurements on viral capsids. To do so, the point force was applied to each vertex perpendicularly to the axis connecting two opposite pentamers. In order to avoid tilting of the capsid when pushing close to the poles, the lowest 10% of vertices of the shell were kept fixed in the simulations. Figure 9 shows the distribution of stretching energy in such an ensemble measurement for a skew (5, 3) and a nonskew (7, 0) structure at $\gamma = 10^6$. Here, each single vertex was indented a distance $\Delta = 0.1R$. For each vertex position on the shell the deformation energy was recorded and averaged over all indentation sites.

Capsids will most likely break in regions of high average deformation energy. Figure 9 shows that the deformation energy is concentrated near the edges of the lower and upper caps. The nonskew capsid design leads to a high concentration of deformation energy close to the pentamers.

A somewhat different ensemble was probed in Fig. 10 where every vertex was indented until material failure occurred. For the skew capsids the forces required to break the shell are much larger than for nonskew capsids. This is in agreement with our finding that skew structures have larger spring constants. Compared to nonskew capsid a larger force is needed to produce a deformation of the same order.

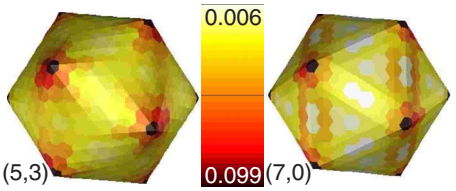

FIG. 9. (Color online) Distribution of the average change of the in-plane deformation energy at an indentation of $\Delta = 0.1R$ for a (5,3) structure (left) and a (7,0) structure (right) at $\gamma = 10^6$. Indentation was perpendicular to the axis spanned by the pentamers at the left and right.

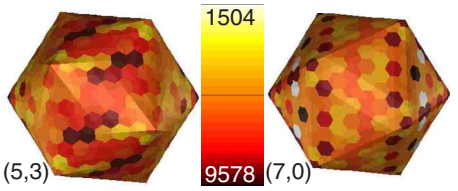

FIG. 10. (Color online) Distribution of rupture forces for a (5,3) structure (left) and a (7,0) structure (right). Force is measured in units of κ_b/R.

E. Capsids under pressure

1. Energetics of packed DNA

In this section we will analyze the influence of DNA packaging on the elastic properties. To do so, we focus on cylindrical capsids representing elongated icosadeltahedra such as the capsids of $\phi 29$ and several T phages. The DNA inside these phages is highly organized. Mechanical and electrostatic interactions force the DNA to form spools [32–34,57]. Purohit *et al.* have discussed in detail the energies associated with different packing geometries [35]. Here, it is simply assumed that the DNA (with length L) is coiled around the cylinder axis. The total energy of this configuration, consisting of electrostatic repulsion and bending energy, in a cylinder of length z and radius R_0 is given by [35]

$$E = \sqrt{3}LF_0(c^2 + cd_s)\exp\left(-\frac{d_s}{c}\right) + \frac{2\pi}{\sqrt{3}}k_bT\xi_p\frac{z}{d_s^2}\ln\left(\frac{R_0}{R}\right). \tag{73}$$

Here, $F_0 \simeq 1.5\times 10^5$ pN/nm^2 is an empirical constant characterizing the strength of electrostatic repulsion, and $c \simeq 0.27$ nm is the screening length. Both F_0 and c depend on the buffer solution and are given in Refs. [35,58] for a 500 mM NaCl solution at 298 K. R is the inner radius of the DNA coil and d_s the spacing between neighboring DNA strands. $\xi_p \simeq 50$ nm is the persistence length of DNA [59] (see also [60] and references therein). For given genome length and geometry, R and d_s are not independent. Their relation is found by minimizing Eq. (73) with respect to R which yields [35]

$$d_s(R) = \left(\frac{2\pi}{\sqrt{3}}\frac{z}{L}(R_0^2 - R^2)\right)^{1/2}. \tag{74}$$

From Eq. (73) the DNA pressure can be calculated. To do so, it assumed that the capsid volume changes isotropically implying that the ratio $z/R_0 \equiv \beta$ is constant. For $\phi 29$ one has $\beta \approx 2$ and the pressure is given by

$$p = -\frac{\partial E}{\partial V} = -\frac{1}{3\pi\beta R_0^2}\frac{\partial E}{\partial R_0}. \tag{75}$$

We consider fixed buffer conditions at constant $c=0.27$ nm and $F_0=1.5\times 10^5$ pN/nm. With Eqs. (74) and (75) the pressure is a function of R_0 and R. The relation between the two radii is given implicitly by the equilibrium condition

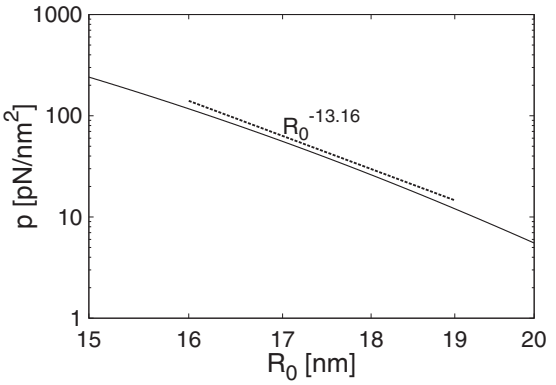

FIG. 11. Internal pressure in phage $\phi 29$ has a much stronger dependence on the external radius R_0 than the R_0^{-3} scaling expected for a hydrostatic pressure contribution to the total energy. The dashed line is a power law fit to the analytical curve (solid line).

$$\frac{\partial E(R,R_0)}{\partial R} = 0. \tag{76}$$

The above equation can be solved numerically for $R(R_0)$, converting Eq. (75) into a function of R_0 only. We have evaluated $p(R_0)$ numerically with the geometrical values specific for $\phi 29$ (radius $R \simeq 20$ nm, cylinder height $z \simeq 40$ nm, and genome length $L \simeq 6.6$ μm). The function $p(R_0)$ is plotted in Fig. 11. The pressure displays a very strong dependence on the outer shell radius. Under the conditions specified above, we observe roughly a $p \sim R_0^{-13}$ scaling whereas for a hydrostatic pressure contribution $(-pV)$ one would expect a R_0^{-3} scaling. Thus, volume compression is strongly inhibited by the electrostatic and mechanical interactions of the DNA coil. For small outer radii or large initial pressures, this suppression effectively acts as a volume constraint.

For the conditions investigated here, the volume changes are of the order of 2% corresponding to a shrinkage of the outer radius of less than 1% (see Fig. 16 below). From Fig. 11 we extract for $\phi 29$ a corresponding pressure increase from 5.5 to 6.5 MPa. In this regime we can therefore consider the pressure to be nearly constant.

The above analysis is only valid for homogeneous volume changes which leave the geometrical aspect ratio constant. However, in a DNA spool pressure is anisotropic since the electrostatic repulsion acts mainly along the spooling axis while the bending forces act in radial direction. From Eq. (73) the parallel and perpendicular components can be computed

$$p_\perp = \frac{1}{2\pi R_0 z}\frac{\partial E}{\partial R_0}, \tag{77}$$

and

$$p_\parallel = \frac{1}{\pi R_0^2}\frac{\partial E}{\partial z}. \tag{78}$$

Replacing d_s by the right-hand side of Eq. (74) we get for the anisotropy α

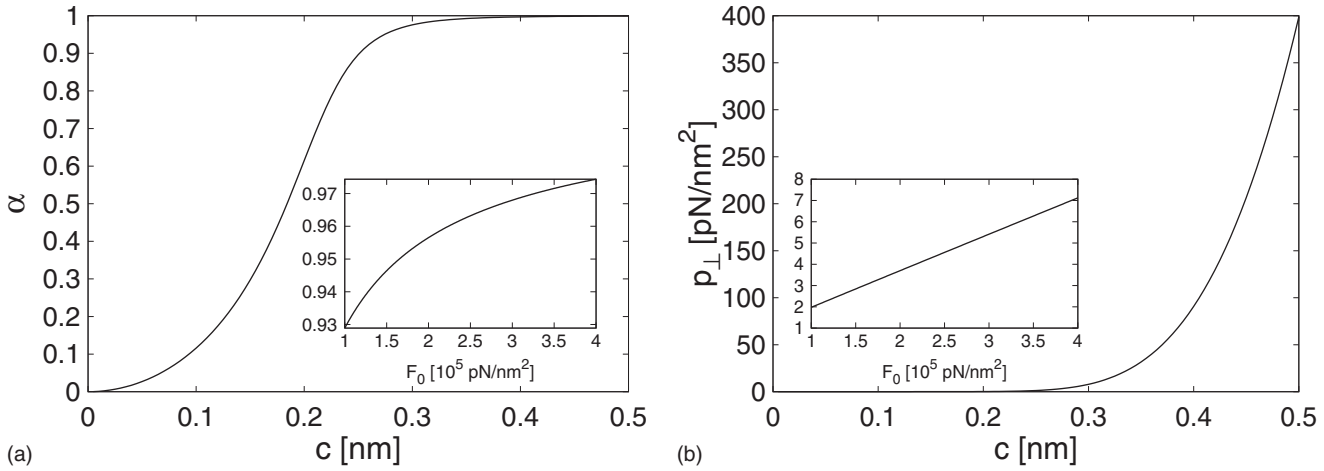

FIG. 12. (a) Ratio α between parallel and perpendicular pressure as a function of the screening length c. Here $\phi 29$ is modeled as a cylindrical container in which the DNA is coiled up. For filled capsids one finds for reasonable (*in vivo*) salt concentrations $0.5 \leqslant \alpha \leqslant 1$. Note that for repulsive electrostatic interactions α is always smaller than 1. (Inset) The F_0 dependence of α. Reasonable values for F_0 range from 0.5 to 3pN/nm^2 [35]. In this range the repulsive strength F_0 has only slight influence on α. (b) Perpendicular pressure as a function of c and F_0. Dilution of the buffer leads to a large increase of the pressure, ultimately bursting the capsid (for parameter values see text).

$$\alpha^{-1} = \frac{R_0^2}{R_0^2 - R^2} + \frac{k_b T \xi_p L \exp(d/c)[R^2 - R_0^2 + 2R_0^2 \ln(R_0/R)]}{2\pi(R_0^2 - R^2)^3 z F_0}. \tag{79}$$

Because the first term in the last equation is always larger than 1 and the second term is always positive for a purely repulsive electrostatic interaction ($F_0 > 0$), α can never exceed 1. This implies that the pressure is always larger in perpendicular direction.

The dependence of the anisotropy of $\phi 29$ on the buffer conditions is shown in Fig. 12(a). For the analysis of the screening length dependence the repulsion strength was fixed at $F_0 = 1.5 \times 10^5$ pN/nm^2. Correspondingly, $c = 0.27$ nm was kept constant to study the F_0 dependence. Under these conditions $\phi 29$ has an anisotropy of $\alpha \simeq 0.97$ implying that $\phi 29$ has hardly any anisotropic pressure distribution despite its (approximately) cylindrical shape. However, dilution of the buffer solution may significantly reduce the screening length giving rise to a larger anisotropy. In this case the increased interstrand repulsion drastically amplifies both axial and perpendicular pressure [see Fig. 12(b)].

Numerically, the presence of the DNA can be taken into account in two fundamentally different ways. (i) An explicit volume energy $-pV$ can be added to the free energy (1) accounting for the work needed to compress the filled capsid. Thus, in this case the total energy of the capsid is given by

$$E = E_b + E_e - pV. \tag{80}$$

This approach is justified by the experimental estimates of the internal pressure of phages like $\phi 29$ or $T4$. Such a description also allows for the inclusion of an anisotropic pressure distribution (see Appendix B). (ii) A volume constraint can be added to Eq. (1). This is justified for large pressures where the strong R_0 dependence of the pressure effectively keeps the volume fixed. The capsid elasticity under such conditions is studied in Sec. IV E 4.

2. Osmotic shock

As discussed above, electrostatic repulsion between neighboring DNA strands contributes to the internal pressure. The strength of this repulsion of course depends on the ionic strength of the buffer solution. Under osmotic shock (with no salt in the surrounding medium) the internal pressure is the highest. In fact, these conditions are used experimentally to extract DNA from viral capsids. Under osmotic shock some viral capsids (e.g., T-even phages) rupture while others (e.g., T-odd phages) stay intact [61,62], indicating that stability depends on details of the capsomer-capsomer interactions.

In this section we analyze the dependence of the stability under osmotic shock on the elastic moduli of the capsid material and the anisotropy of DNA packing. The numerical simulation of capsids subjected to an (anisotropic) internal pressure are based on the discretization of the volume energy derived in Sec. IV B.

An estimate for the maximal sustainable pressure can be obtained from the discrete description (see Sec. III) of viral capsids assuming that there is some maximum sustainable strain. In first order an increased pressure leads merely to an isotropic expansion of the shell. Because the bending energy is scale invariant the deformation is set by the equilibrium of volume energy $-pV$ and stretching energy. A shell with initial radius R that has been inflated to a radius R' experiences an expanding force

$$F_p = 4\pi p R'^2, \tag{81}$$

and a counteracting, restoring force arising from the stretching energy

$$E_e = \frac{\sqrt{3}}{4} \kappa_e B [l_0 - l(R')]^2. \tag{82}$$

Here, l_0 is the initial length of a bond, B is the number of bonds, and $l(R')$ denotes the length of a bond in the inflated

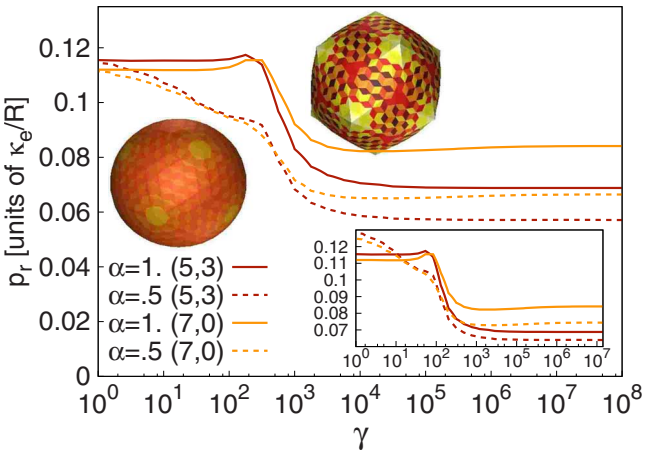

FIG. 13. (Color online) Rupture pressure as function of γ for skew [red (dark gray) line] and nonskew [orange (light gray) line] structures. The triangulation number is $T=49$. Solid lines correspond to isotropic pressure while dashed lines correspond to $\alpha=0.5$. Both the mean pressure, averaged over the capsid surface (large figure), and the maximum of the pressure field (inset) are shown. The inset structures visualize the strain distribution in the skew capsid at $p=0.1\kappa_e/R$ for $\gamma=10$ (left) and $\gamma=10^5$ (right). The scale ranges from no strain [yellow (white)] to 6.5% [red (black)]. Orange (light gray) corresponds to approximately 4.5% strain. Above the buckling threshold the pressure-induced strain is localized close to the pentamers, reducing the critical pressure significantly.

shell. If the triangulation is equilateral the number of triangles is

$$N=\frac{16}{\sqrt{3}}\pi\frac{R^2}{l_0^2}. \tag{83}$$

A facet shares each of its three edges with its adjacent facet and therefore $N=2B/3$. For a given shell radius R' the length of a bond is then given by

$$l^2(R')=\frac{8\sqrt{3}}{B}\pi R'^2, \tag{84}$$

and the restoring force becomes

$$F_e=\frac{dE_e}{dR'}=12\pi\kappa_e(R'-R). \tag{85}$$

Equilibrium can only be found for sufficiently low pressures, i.e., for $p\leqslant p_{\max}$ with the maximal sustainable pressure

$$p_{\max}\equiv\frac{3}{4}\frac{\kappa_e}{R}. \tag{86}$$

For higher pressures the inflating force prevails and R' expands to infinity. The relative bond length change at pressure $p_{\max}$ is given by

$$\frac{l-l_0}{l_0}=\frac{p}{3}. \tag{87}$$

Given a fixed maximal strain, the rupture pressure is a constant for all γ. For our particular choice of the critical strain we have $p_r=0.135\kappa_e/R$.

Numerically, we have increased the mean pressure in steps of $\delta p=0.001\kappa_e/R$. For each step the maximal strain was recorded. This was done systematically for a wide range of γ. The data collected in this way yields the strain as function of γ and the mean pressure p averaged over the capsid surface. Figure 13 shows contour plots of these data at a strain value of 4.5%. For isotropic packing the rupture pressure agrees nicely with the estimated value for FvK numbers below 1000. Above this value shell buckling induces a dramatic decrease of capsid stability. This behavior can be attributed to an inhomogeneous strain distribution above the buckling threshold (see inset in Fig. 13). Here, the pressure mainly deforms the soft icosahedral facet, thus leading to high local strain on the facet centers.

For anisotropic pressure the stability is further decreased; see the inset of Fig. 13, which shows the maximum of the pressure distribution (i.e., $p_\perp$) as function of γ. The curves for anisotropic pressure are simply shifted upward by a constant factor $4/[(4-\pi)\alpha+\pi]$ [see Eq. (B2)]. But still the rupture (peak) pressure is lower for anisotropic packing.

3. Point forces

In many phages the DNA packaging motor is located at a pentameric position. Therefore, it is reasonable to assume

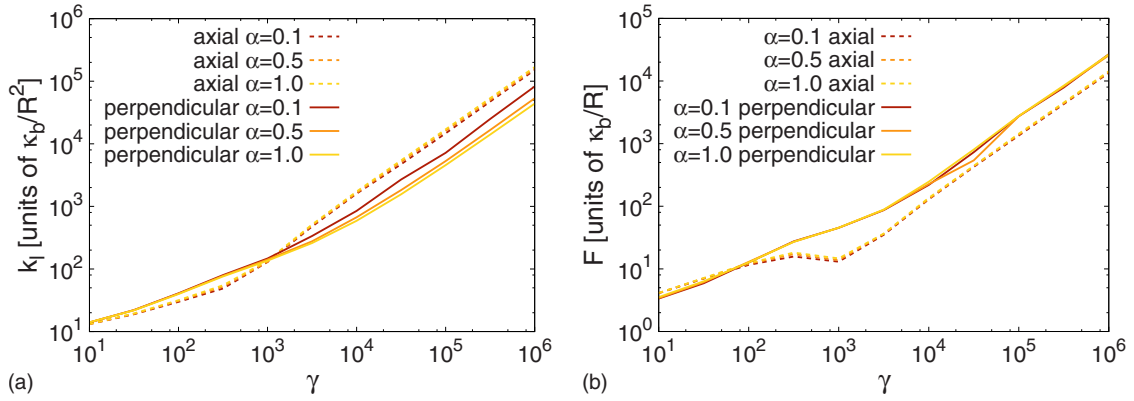

FIG. 14. (Color online) Elastic response of capsid with internal pressure $p=0.02\kappa_e/R$. Different degrees of anisotropy and different loading directions are compared. γ dependence of the linear spring constants (a) and the rupture force (b) of densely packed capsids are shown. Both depend mainly on the FvK numbers only. Neither the loading direction nor the anisotropy have a significant effect.

that the DNA spools around the axis defined by the motor and its opposite pentamer. To mimic this in our simulations, the axis of cylindrical symmetry is defined by the positions of two opposite pentamers. In our simulations we set $p=0.02\kappa_e/R$. This is less than the values obtained for filled $\phi 29$ capsids [29] ($p=0.06\kappa_e/R$) since at $p=0.06\kappa_e/R$ a moderate anisotropy of $\alpha=0.5$ would already lead to rupture (see Fig. 13). We have studied two different types of loading: parallel and perpendicular to the axis of anisotropy. Due to the capsid geometry, axial (perpendicular) loading corresponds to the indentation of pentamers (hexamers).

At high pressures the circumferential stress at the fivefold disclinations is balanced by the volume contribution pV. Thus, pentamers do not form rigid buckles and hexamers remain flat. For example, the DNA pressure of 6 MPa in $\phi 29$ phages ($\gamma \approx 1778$) reduces the asphericity $a \equiv \langle \Delta R^2 \rangle / \langle R \rangle^2$ from $a \simeq 1.4 \times 10^{-3}$ for an empty capsid to $a \simeq 0.6 \times 10^{-3}$. Thus, hexamers and pentamers behave similarly, in particular their elastic response is nearly identical at high internal pressure. Figure 14(a) shows that a moderate pressure $p=0.02\kappa_e/R$ is sufficient to blur the spatial variations of shell stiffness. A similar effect is observed for the rupture force [see Fig. 14(b)]. Most astonishingly, the anisotropy of the pressure field has no significant influence on the local spring constants and the shell stability (see Fig. 14). Even an extreme anisotropy of $\alpha=0.1$ does not lead to any noticeable effect.

Compared to empty capsids an internal pressure increases both force and indentation needed to disrupt the shell see (Fig. 15). This is easy to understand: since the filled capsid is initially inflated the material is stretched. Therefore, one has to indent more deeply in order to reach the critical compression of 4.5%.

As in Sec. IV C the numerical result can be compared to experimental data to get estimates for the bulk elastic moduli. The results for viruses, for which experimental values were available, are summarized in Table II. Filled λ phages have the same Young's modulus as empty capsid, implying that the change in the elastic response can be explained by the internal pressure alone. In contrast, the comparison between numerics and experiments for CCMV yields different Young's moduli for filled and empty capsids. Even more astonishingly, experimentally the filled MVM virus shows a trimodal spring constant distribution, while the empty capsid has a uniform elastic response [10]. These findings disagree with our numerical results which indicate that the elastic response of pentamers and hexamers becomes similar. A possible explanation could be that apart from the purely mechanical reinforcement, DNA has also a strong biochemical effect on shell stability. The estimated rupture forces for these viruses are summarized in Table III. As for the empty capsids, the rupture force is slightly larger in the numerical simulations.

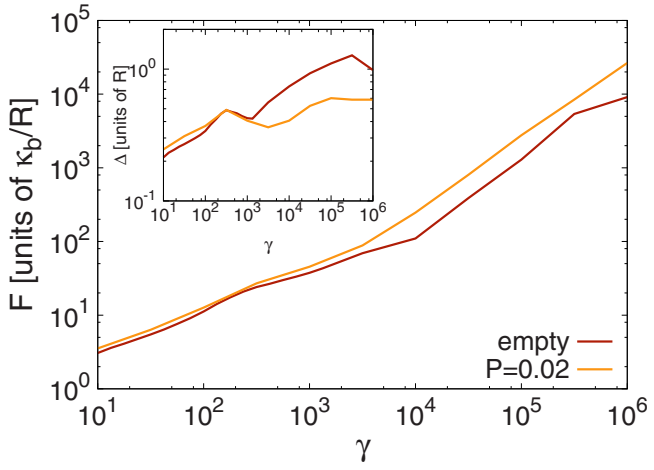

FIG. 15. (Color online) Force (main panel) and indentation (inset) needed to break a (5,3) shell. Filled capsids [orange (light gray) curve] need a somewhat higher rupture force than empty shells [red (dark gray) curve], due to initial pressure-induced stretching of the capsid material. Correspondingly, the rupture indentation is also increased.

4. Constrained volume

Numerically, a volume constraint can be implemented by introducing an energetic penalty for any deviation from the initial volume V_0, given by the potential

$$E_v = k_v (V_0 - V)^2, \tag{88}$$

where V is the volume of the shell. In the simulations the Lagrange multiplier was chosen to be $k_v=100\kappa_e$. It is important to note the k_v must not be too large since otherwise the total energy is dominated by E_v and the deformation energy E_b+E_e is only minimized with poor precision. As the insets in Fig. 16 show, with the chosen value of k_v a constant volume is ensured.

Representative force distance curves for $\gamma = 10, 10^2, 10^3, 10^4$ are shown in Fig. 16 and compared to the results for empty shells and shells under pressure ($p=0.02\kappa_e/R$). For $\gamma<10$ and small indentations the force-distance behavior agrees with that of empty shells. For larger γ the forces needed to indent pressurized capsids are generally somewhat larger (see Fig. 16).

From Fig. 16 we conclude that the constraint on the enclosed volume does not have a significant influence on the

TABLE III. Experimental (F_r) and numerical ($F_r^{(n)}, \Delta_r^{(n)}$) rupture data. The numerical values are determined for the indentation of hexamers. The rupture forces of filled capsids are discussed in Sec. IV E. As far as we know, no experimental data are available for filled $\phi 29$. The tolerance in the numerical rupture forces for CCMV is due to the tolerance in the bending stiffness, which arises from the numerically observed bimodal spring constant distribution.

	F_r (nN)	$F_r^{(n)}$ (nN)	$\Delta_r^{(n)}$ (nm)
$\phi 29$			
Empty	1.0	1.0	7.7
Filled		1.8	6.8
λ			
Empty	0.8	1.4	13.2
Filled	1.6	2.02	10.6
CCMV			
Empty	0.63	0.7 ± 0.1	5.2
Filled	0.8	1.1 ± 0.2	5.9

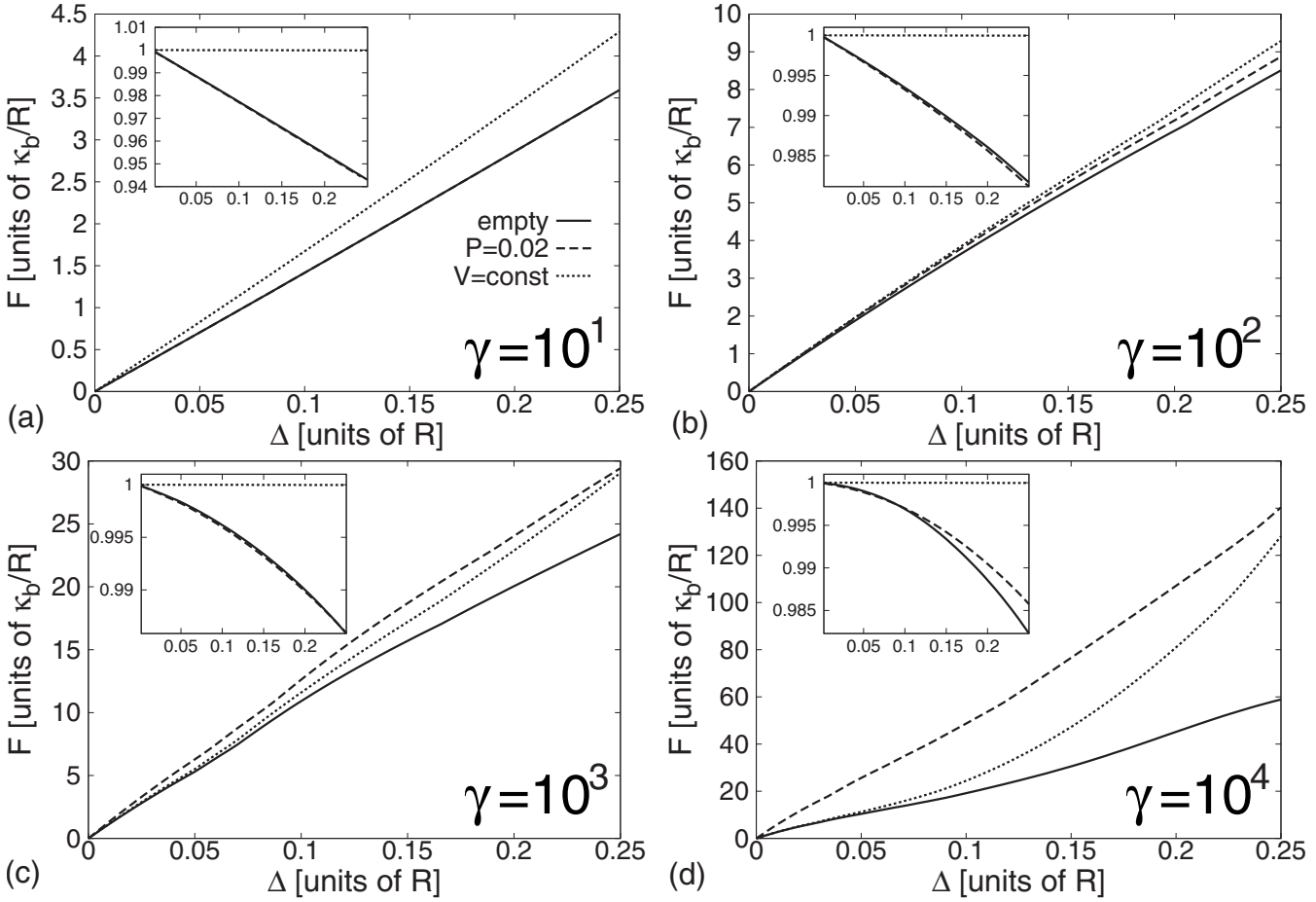

FIG. 16. Force-distance curves for empty (solid lines) capsids and filled capsids. The presence of DNA is modeled either by a pressure contribution with $p=0.02\kappa_e/R$ (dashed lines) or a volume constraint (dotted lines). In (a) and (b) the dashed and solid curves lie on top of each other. Deviations between empty capsids and those with conserved volume become apparent only for indentation $\Delta \sim 0.1R$. Interestingly, for $\gamma > 10$ capsids under DNA pressure are generally stiffer than those with a fixed volume. The insets show the dependence of the enclosed volume on the indentation depth. Clearly, the volume is not conserved for empty shells and shells with internal pressure.

linear spring constants. This can be explained as follows: The spring constant is taken at small indentations where the volume does not change significantly and the volume constraint Eq. (88) has only little effect. Minor deviations from the empty shell behavior arise for small γ [see Fig. 16(a)], where the scale-invariant bending energy dominates. As already discussed in Sec. II D, in this regime an empty shell simply responds with a global shrinkage to external forces. When the enclosed volume is fixed the shell has to transform its shape, thus inducing additional curvature leading to a higher spring constant. For larger γ these induced deformations are strongly localized even for empty shells and the volume constraint is less significant in this regime.

However, significant differences in the elastic behavior occur at larger indentations. Here, the spring constants (given by the *local* slopes of the F-Δ curve) are generally somewhat larger. This can be understood in the following picture. To preserve constant cross-sectional area, the local compression at the point of loading must be compensated by an additional expansion of the equatorial area. Therefore, the influence of the volume constraint becomes more apparent for larger γ. An interesting phenomenon is observed for $\gamma=10^4$, where the volume constraint leads to a nonlinear stiffening of the shell, resulting in a concave force distance curve [see Fig. 16(d)].

Figure 17(a) shows the rupture force as function of γ. For the rupture force we observe a clear γ^1 scaling for $\gamma > 1000$. Figure 17(b) shows that in this γ range rupture occurs in the inverted shape at a constant indentation $\Delta_r \approx 0.4R$. From the insets in Fig. 17(a) it is apparent that the main rupture mechanism in filled capsids is stretching of the material, in contrast to empty shells. For small $\gamma < 100$, where rupture occurs in the noninverted regime, the material fails due to equatorial expansion. For higher γ (after the inversion transition) the shell breaks because of strong stretching close to the point of loading.

V. SUMMARY AND OUTLOOK

The mechanical properties of viral capsids have recently attracted much experimental interest. In this work we have developed analytical and numerical methods to complement these studies and to make theoretical predictions about the elastic properties of empty and filled, skew and chiral capsids.

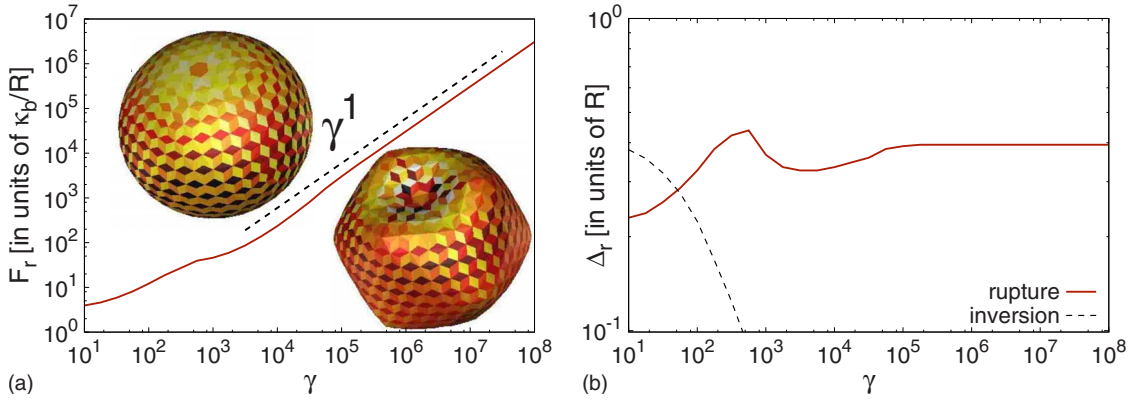

FIG. 17. (Color online) (a) Rupture force for capsids with volume constraint. The insets show the strain distribution in ruptured structures at $\gamma=10$ and 1000. The color code ranges from yellow (white) (4.5% compression) to red (black) (4.5% expansion). The main rupture mechanism in filled capsids with fixed internal volume is material *stretching*. (b) Rupture indentation and numerically determined inversion threshold as function of γ. Above $\gamma\approx 100$ rupture already occurs in the inverted regime. Correspondingly, the $\gamma=1000$ structure shown in the inset is slightly inverted. Above the buckling threshold, rupture occurs at a constant depth $\Delta\approx 0.4R$.

Within a continuum approximation, which ignores the presence of disclinations, we are able to identify a linear and a nonlinear response regime. The properties of these two regimes can already be analyzed in a simple scaling analysis of the force-indentation relation. A variational approach, however, puts these findings on more solid grounds. By expanding the force-induced deformation up to second order we find an exact formula for the functional dependence of the linear spring constant on the FvK number γ which differs from the simple square-root law expected from scaling arguments for small γ. Assuming a critical strain at which the shell breaks, we find that the rupture indentation is a constant for all FvK numbers.

The mechanics at larger indentations and for large γ can only be investigated numerically. In the latter case the mechanical properties are dominated by the disclinations which have to be taken explicitly into account. The arrangement of the disclinations can be varied giving rise to skew and nonskew capsids.

We have compared the elastic properties of different capsid designs. Generally, skew capsids have lower deformation energy in the buckled ground state than nonskew ones. This might explain why some viruses (such as PBCV 1 and CIV) have a skew capsomer arrangement.

By simulating viral capsids under small deformations, we find that for FvK numbers $\gamma<1000$ the spring constants of both skew and nonskew agree well with the continuum results. Above $\gamma>1000$, pentamers become stiffer and hexamers softer. Interestingly, skew capsids appear to be stiffer than nonskew ones.

In our simulations the mechanical limits of viral shells can be probed in an ensemble where every capsomer is indented. In doing so, we find surprisingly strong deviations from the expected constant rupture indentation even in the linear regime, indicating that already for small indentations the presence of disclination cannot be neglected. The capsid design has no influence on the rupture behavior. Also, for these ensemble measurements skew capsids are more rigid and more stable than nonskew capsids. In particular, skew capsids have higher rupture forces than nonskew ones.

Finally, we have studied the influence of internal pressure arising from packed DNA on capsid mechanics. At high pressure the elastic response of hexamers and pentamers becomes similar. An anisotropic pressure distribution leads to a lower rupture pressure. However, anisotropy has hardly any influence on the mechanical behavior under point force loading.

Generally these findings indicate that the disclinations have quite an influence on the elastic properties even below the buckling threshold. For a deeper understanding it will become important to find ways of including these in the analytical description. Possibly, these can be done by extending the analysis of Ref. [37] to curved surfaces or by deriving the shape equation for an icosahedral surface. However, none of these approaches seem to be straightforward.

APPENDIX A: COMPARISON OF DISCRETIZATION SCHEMES

Here, we compare the different discretization schemes for the bending energy.

1. Heisenberg discretization scheme

A numerically very efficient representation of the mean curvature uses the difference between the unit normals of two neighboring facets. The bending energy is then given by a Heisenberg-type Hamiltonian [63],

$$E_b^{\mathrm{disc}} = \frac{\tilde{\kappa}_b}{2}\sum_{\langle i,j\rangle} |\boldsymbol{n}_i - \boldsymbol{n}_j|^2 = \tilde{\kappa}_b \sum_{\langle i,j\rangle} (1 - \boldsymbol{n}_i \cdot \boldsymbol{n}_j). \tag{A1}$$

Here, the sum extends over all neighboring pairs of facets $\langle i,j\rangle$. In the limit of a very fine triangulation (A1) represents the continuous Helfrich Hamiltonian [37],

$$E_b^{\mathrm{disc}} \to 2\kappa_b \int dA\, H^2 - \frac{1}{2}K. \tag{A2}$$

In simple geometries, such as cylinders or spheres, it is easy to calculate directly both the discretized and the continuous

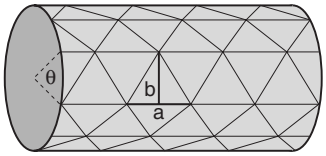

FIG. 18. A cylinder can be triangulated in such a way that its surface is subdivided into bands parallel to the cylinder axis. For such a triangulation the relation between numerical and continuous bending energy can be easily calculated.

bending energy. A direct comparison then yields the numerical relation between $\tilde{\kappa}_b$ and κ_b [64].

First consider a sphere covered with N nearly equilateral triangles with edge length a and area $\sqrt{3}a^2/4$. The distance between the midpoints of two neighboring facets is $h=a/\sqrt{3}$. Since $h=2R\sin(\theta/2)\approx R\theta$ the angle between two neighboring normal vectors is $\theta=a/\sqrt{3}R$. The number of edges is $E=3/2N$ where $N=16\pi R^2/\sqrt{3}a^2$, and the discretized bending energy is

$$E_b^{\mathrm{disc}} = \tilde{\kappa}_b E\left(1-\cos\frac{a}{\sqrt{3}R}\right) \overset{a\to 0}{\to} \frac{4\pi}{\sqrt{3}}\tilde{\kappa}_b. \tag{A3}$$

Comparison of this result with the continuous bending energy $F_b=4\pi\kappa_b$ yields

$$\tilde{\kappa}_b = \sqrt{3}\kappa_b. \tag{A4}$$

Numerical simulations with spheres with up to 4000 vertices have confirmed the relation $E_b^{\mathrm{disc}} \simeq 7.25\tilde{\kappa}_b$ (data not shown).

However, one should be aware that Eq. (A4) is valid only if all triangles are nearly equilateral and the mesh size becomes infinitely small. To illustrate this consider a triangulated cylinder of length L as depicted in Fig. 18. Within a band all normal vectors are parallel. Hence, only the longitudinal edges contribute to the discrete bending energy. Generally, the number of bands N_φ can be chosen independently from the number of longitudinal edges per band N_z. The angle between two neighboring bands is $\theta=2\pi/N_\varphi$. As an specific example, for isosceles triangles with height b and base length a one has $N_\varphi \approx 2\pi R/b$ and $N_z=L/a$. In the limit of an infinitesimal triangulation $N_z, N_\varphi \to \infty$, $a/b=$const, the discrete bending energy becomes

$$E_b^{\mathrm{cyl}} = \tilde{\kappa}_b N_z N_\varphi\left(1-\cos\frac{2\pi}{N_\varphi}\right) \to \tilde{\kappa}_b 2\pi^2\frac{N_z}{N_\varphi} = \tilde{\kappa}_b\frac{\pi L}{R}\frac{b}{a}. \tag{A5}$$

Comparing this result with the continuous bending energy, $E_b=\kappa_b\pi L/R$ yields $\tilde{\kappa}_b/\kappa_b=a/b$. Since the lengths a and b can be chosen independently this ratio is arbitrary. Therefore, the discretization (A1) together with Eqs. (A4) (for spheres) and (A5) (for cylinders) is appropriate for the numerical treatment of membranes only when a high in-plane rigidity gives preference to an equilateral triangulation. At the latest when the structure is strongly deformed an equilateral triangulation can no longer be guaranteed. This is the case for small γ where the weak in-plane elastic part of the total energy does not impose any restrictions on the bond length. In this regime the assumption of an equilateral mesh is strongly violated since the mesh size becomes very small near the pentamers to adopt a more spherical shape. We have compared the quality of both discretizations calculating the spring constants of triangulated spherical shells for γ between 1 and 100. As can be seen from Fig. 19, the Heisenberg discretization is not capable of reproducing the spring constants correctly.

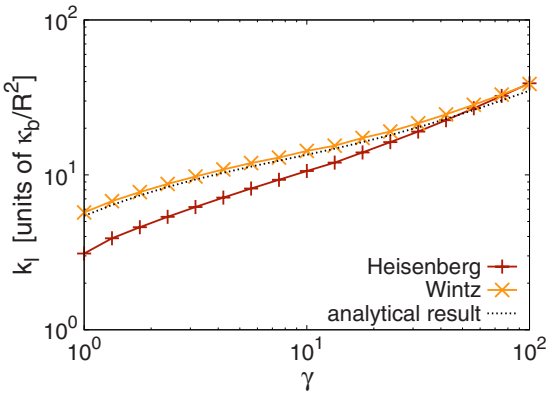

FIG. 19. (Color online) The linear spring constant of triangulated spherical shells follows nicely the analytical curve (dotted black line) when the Wintz discretization scheme is used. In the simpler discretization scheme k_l is somewhat lower. For $\gamma<100$ the simple scheme is no longer valid due to strong deviations from the equilateral triangulation. However, for $\gamma>100$ both discretization schemes agree well with the analytical curve Eq. (60).

2. Discretization scheme by Wintz *et al.*

In our study we consider strongly deformed spheres and in this case the triangulation is, in general, no longer equilateral and the discretization scheme (A1) is no longer valid. Fortunately, there is an alternative approach to the discretization of the bending energy, that makes use of a direct geometrical interpretation of the mean curvature H [36]. When the points on a surface are moved along the local surface normal by a distance δ, the area of a surface patch changes by $2\delta/H+O(\delta^2)$. For the discretized surface this gives rise to the representation of the mean curvature of the ith edge [36] as given by relation (70). As can be seen from Fig. 19, simulations using this discretization scheme give a much better agreement with the analytical spring constant. Alternatively, methods using dual lattices could be employed (see Ref. [64]).

APPENDIX B: NUMERICAL IMPLEMENTATION OF ANISOTROPY

Generally, pressure is implemented numerically by taking into account an additional contribution $-pV$ to the total energy. For our numerical simulations of pressure distributions with anisotropy α we assume a functional dependence of the form

$$p(\theta) = p_{\parallel}\left(1+\frac{1-\alpha}{\alpha}\sin\theta\right). \tag{B1}$$

Here, the angle $0\leqslant\theta\leqslant\pi$ is measured relative to an axis of anisotropy $\boldsymbol{a}$. We define the mean pressure $\bar{p}$ as the average of (B1) over the surface, given by

$$\bar{p} = p_{\parallel}\left(1 + \frac{\pi}{4}\frac{1-\alpha}{\alpha}\right). \tag{B2}$$

The energetic contribution of an anisotropic pressure is

$$E_v = -\int dV\, p(\theta). \tag{B3}$$

Numerically, this integral is approximated by a sum over all vertices i,

$$E_v^{\mathrm{disc}} = p_{\parallel}\sum_i \left(1 + \frac{1-\alpha}{\alpha}\frac{|\boldsymbol{x}_i \times \boldsymbol{a}|}{|\boldsymbol{x}_i||\boldsymbol{a}|}\right)V_i. \tag{B4}$$

Here, $\boldsymbol{x}_i$ is the position of the vertex i and $\sin\theta$ is given by a vector product of position vector $\boldsymbol{x}_i$ and axis $\boldsymbol{a}$. The volume V_i is then

$$V_i = \frac{1}{18}\sum_{\langle j,j'\rangle} |\boldsymbol{x}_i \cdot (\boldsymbol{k}_j^i \times \boldsymbol{k}_{j'}^i)|. \tag{B5}$$

With this definition the sum over all V_i results in the total volume of the capsid. Here, $\boldsymbol{k}_j^i$ is the direction of the jth edge connected to the vertex i. The sum extends over all pairs of neighboring edges of vertex i.

[1] F. Gerbal, V. Laurent, A. Ott, M. F. Carlier, P. Chaikin, and J. Prost, Eur. Biophys. J. **29**, 134 (2000).
[2] R. Tharmann, M. M. A. E. Claessens, and A. R. Bausch, Phys. Rev. Lett. **98**, 088103 (2007).
[3] A. Micoulet, J. P. Spatz, and A. Ott, ChemPhysChem **6**, 663 (2005).
[4] M. Sotomayor and K. Schulten, Science **316**, 1144 (2007).
[5] I. Ivanovska, P. de Pablo, B. Ibarra, G. Sgalari, F. MacKintosh, J. Carrascosa, C. Schmidt, and G. L. Wuite, Proc. Natl. Acad. Sci. U.S.A. **101**, 7600 (2004).
[6] W. S. Klug, R. F. Bruinsma, J.-P. Michel, C. M. Knobler, I. L. Ivanovska, C. F. Schmidt, and G. J. L. Wuite, Phys. Rev. Lett. **97**, 228101 (2006).
[7] R. M. Atlas, *Principles of Microbiology* (Wm. C. Brown, Dubuque, 1998).
[8] N. Kol, M. Gladnikoff, D. Barlam, R. Z. Shneck, A. Rein, and I. Rousso, Biophys. J. **91**, 767 (2006).
[9] J. Michel, I. Ivanovska, M. Gibbons, W. Klug, C. Knobler, G. L. Wuite, and C. Schmidt, Proc. Natl. Acad. Sci. U.S.A. **103**, 6184 (2006).
[10] C. Carrasco, A. Carreira, I. A. T. Schaap, P. A. Serena, J. Gomez-Herrero, M. G. Mateu, and P. J. de Pablo, Proc. Natl. Acad. Sci. U.S.A. **103**, 13706 (2006).
[11] F. Crick and J. Watson, Nature (London) **177**, 473 (1956).
[12] D. Caspar and A. Klug, Cold Spring Harb Symp. Quant Biol. **27**, 1 (1962).
[13] A. Klug and D. L. D. Caspar, Adv. Virus Res. **7**, 225 (1960).
[14] P. Horne and R. W. Wildy, Virology **15**, 348 (1961).
[15] N. Nandhagopal, A. A. Simpson, J. R. Gurnon, X. Yan, T. S. Baker, M. V. Graves, J. L. Van Etten, and M. G. Rossmann, Proc. Natl. Acad. Sci. U.S.A. **99**, 14758 (2002).
[16] X. Yan, N. Olson, J. Van Etten, M. Bergoin, M. Rossmann, and T. Baker, Nat. Struct. Biol. **7**, 101 (2000).
[17] C. Xiao, P. R. Chipman, A. J. Battisti, V. D. Bowman, P. Renesto, D. Raoult, and M. G. Rossmann, J. Mol. Biol. **353**, 493 (2005).
[18] B. K. Ganser-Pornillos, U. K. von Schwedler, K. M. Stray, C. Aiken, and W. I. Sundquist, J. Virol. **78**, 2545 (2004).
[19] Y. Tao, N. H. Olson, W. Xu, D. L. Anderson, M. G. Rossmann, and T. S. Baker, Cell **95**, 431 (1998).
[20] M. Yanagida, J. Mol. Biol. **109**, 515 (1977).
[21] T. T. Nguyen, R. F. Bruinsma, and W. M. Gelbart, Phys. Rev. E **72**, 051923 (2005).
[22] T. T. Nguyen, R. F. Bruinsma, and W. M. Gelbart, Phys. Rev. Lett. **96**, 078102 (2006).
[23] Z. Zhang, H. T. Davis, and D. M. Kroll, Phys. Rev. E **48**, R651 (1993).
[24] J. Lidmar, L. Mirny, and D. R. Nelson, Phys. Rev. E **68**, 051910 (2003).
[25] M. Buenemann and P. Lenz, Proc. Natl. Acad. Sci. U.S.A. **104**, 9925 (2007).
[26] M. Widom, J. Lidmar, and D. R. Nelson, Phys. Rev. E **76**, 031911 (2007).
[27] F. Dubreuil, N. Elsner, and A. Fery, Eur. Phys. J. E **12**, 215 (2003).
[28] N. Elsner, F. Dubreuil, R. Weinkamer, M. Wasicek, F. Fischer, and A. Fery, Prog. Colloid Polym. Sci. **132**, 117 (2006).
[29] D. E. Smith, S. J. Tans, S. B. Smith, S. Grimes, D. L. Anderson, and C. Bustamante, Nature (London) **413**, 748 (2001).
[30] A. Evilevitch, L. Lavelle, C. M. Knobler, E. Raspaud, and W. M. Gelbart, Proc. Natl. Acad. Sci. U.S.A. **100**, 9292 (2003).
[31] S. Tzlil, J. T. Kindt, W. M. Gelbart, and A. Ben-Shaul, Biophys. J. **84**, 1616 (2003).
[32] W. C. Earnshaw and S. C. Harrison, Nature (London) **268**, 598 (1977).
[33] M. Cerritelli, N. Cheng, A. Rosenberg, C. McPherson, F. Booy, and A. Steven, Cell **91**, 271 (1997).
[34] C. R. Locker, S. D. Fuller, and S. C. Harvey, Biophys. J. **93**, 2861 (2007).
[35] P. K. Purohit, J. Kondev, and R. Phillips, Proc. Natl. Acad. Sci. U.S.A. **100**, 3173 (2003).
[36] W. Wintz, Ph.D. thesis, Universität Potsdam, 1997.
[37] H. S. Seung and D. R. Nelson, Phys. Rev. A **38**, 1005 (1988).
[38] A. Šiber, Phys. Rev. E **73**, 061915 (2006).
[39] G. A. Vliegenthart and G. Gompper, Biophys. J. **91**, 834 (2006).
[40] L. Landau and E. Lifshitz, *Theory of Elasticity* (Pergamon, New York, 1975).
[41] E. Kreyszig, *Differential Geometry* (Dover, New York, 1991).
[42] P. Lenz and D. R. Nelson, Phys. Rev. E **67**, 031502 (2003).
[43] G. Kaye and T. Laby, *Tables of Physical and Chemical Constants* (Longman, London, 1993).

[44] N. A. Waterman and M. F. Ashby, *Elsevier Materials Selector* (Elsevier Applied Science, London, 1992).
[45] D. Boal, *Mechanics of the Cell* (Cambridge University Press, Cambridge, U.K., 2002).
[46] I. S. Gradshteyn and I. M. Ryshik, *Table of Integrals, Series and Products* (Academic Press, New York, 1980).
[47] Computer code MATHEMATICA, Version 6.0 (Wolfram Research, Inc., Champaign, IL, 2007).
[48] E. Reissner, J. Math. Phys. (Cambridge, Mass.) **25**, 80 (1946).
[49] G. Gompper and D. M. Kroll, J. Phys. Condens. Matter **9**, 8795 (1997).
[50] W. Press, S. A. Teukolsky, W. T. Vetterling, and B. P. Flannery, *Numerical Recipes in C* (Cambridge University Press, Cambridge, U.K., 1992).
[51] N. Cheng, B. L. Trus, D. M. Belnap, W. W. Newcomb, J. C. Brown, and A. C. Steven, J. Virol. **76**, 7855 (2002).
[52] I. Ivanovska, G. Wuite, B. Jonsson, and A. Evilevitch, Proc. Natl. Acad. Sci. U.S.A. **104**, 9603 (2007).
[53] J. A. Speir, S. Munshi, G. Wang, T. S. Baker, and J. E. Johnson, Structure (London) **3**, 63 (1995).
[54] T. Dokland and H. Murialdo, J. Mol. Biol. **233**, 682 (1993).
[55] A. L. Llamas-Saiz, M. Agbandje-McKenna, W. R. Wikoff, J. Bratton, P. Tattersall, and M. G. Rossmann, Acta Crystallogr., Sect. D: Biol. Crystallogr. **53**, 93 (1997).
[56] M. Yeager, E. M. Wilson-Kubalek, S. G. Weiner, P. O. Brown, and A. Rein, Proc. Natl. Acad. Sci. U.S.A. **95**, 7299 (1998).
[57] J. Kindt, S. Tzlil, A. Ben-Shaul, and W. M. Gelbart, Proc. Natl. Acad. Sci. U.S.A. **98**, 13671 (2001).
[58] V. A. Parsegian, R. P. Rand, N. L. Fuller, and D. C. Rau, Methods Enzymol. **127**, 400 (1986).
[59] J. B. Hays, M. E. Magar, and B. H. Zimm, Biopolymers **8**, 531 (1969).
[60] R. H. Austin, J. P. Brody, E. C. Cox, T. Duke, and W. Volkmuth, Phys. Today **50** (2), 32 (1997).
[61] T. F. Anderson, J. Appl. Phys. **21**, 70 (1950).
[62] S. P. Leibo, E. Kellenberger, C. Kellenberger–van der Kamp, T. G. Frey, and C. M. Steinberg, J. Virol. **30**, 327 (1979).
[63] Y. Kantor and D. R. Nelson, Phys. Rev. Lett. **58**, 2774 (1987).
[64] G. Gompper and D. M. Kroll, J. Phys. I **6**, 1305 (1996).